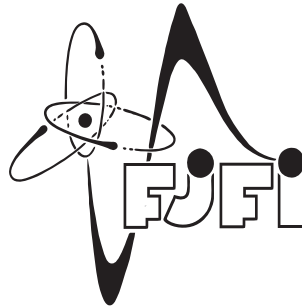


CZECH TECHNICAL UNIVERSITY IN PRAGUE
FACULTY OF NUCLEAR SCIENCES AND PHYSICAL ENGINEERING



DIPLOMA THESIS

EXPLORATION OF KINETIC PROCESSES IN THE LUNAR WAKE

Bc. Martin Jílek

Supervisor: Ing. Pavel Trávníček, Ph.D.

May 6, 2011

Acknowledgements

I would like to thank my supervisor Pavel Trávníček for introducing me to space plasma problematics, valuable advices, and providing me the simulation code. I also thank Ondřej Šebek and Štěpán Štverák, who helped me with technical aspects of simulations performing. Last but not least, I would like to thank my wife Petra Jílková for patient support and careful reading a previous version of this thesis.

Prohlášení

Prohlašuji, že jsem svou diplomovou práci vypracoval samostatně a použil jsem pouze podklady uvedené v příloženém seznamu.

Nemám žádný důvod proti užití tohoto školního díla ve smyslu §60 Zákona č. 121/2000 Sb., o právu autorském, o právech souvisejících s právem autorským a o změně některých zákonů (Autorský zákon).

Declaration

I declare that I wrote my diploma thesis independently and exclusively with the use of cited bibliography.

I agree with the usage of this thesis under the Act 121/2000 (Copyright Act).

Praha, May 6, 2011

Martin Jílek

Dedicated to Marta Jílková and Jaroslav Jílek, my parents . . .

Název práce: **Studium kinetických procesů v lunárním chvostu**

Autor: Martin Jílek

Obor: Matematické inženýrství

Druh práce: Diplomová práce

Vedoucí práce: Ing. Pavel Trávníček, Ph.D., Astronomický ústav AV ČR, Praha

Abstrakt: Studujeme jevy spojené s odrazy protonů slunečního větru na měsíčním povrchu. Provádíme několik dvourozměrných hybridních simulací s protony jako částicemi a elektrony jako tekutinou. Meziplanetární magnetické pole je kolmé na simulační rovinu. Výsledky ukazují vznik chvostu za překážkou s dutinou neobsahující plazma uprostřed obklopenou nízko- frekvenčními vlnami šířícími se směrem od dutiny. Jsou diskutovány vlastnosti a mechanismus vzniku těchto vln. Dále studujeme dynamiku odražených protonů a jejich vliv na prostředí plasmatu v okolí Měsíce. Různé modely odrazu jsou porovnány s in-situ měřeními japonské družice SELENE (Kaguya).

Klíčová slova: lunární chvost, hybridní simulace, magnetosonické vlny.

Title: **Exploration of kinetic processes in the lunar wake**

Author: Martin Jílek

Abstract: We study the phenomena associated with the solar wind protons reflections on the lunar surface. We perform several two-dimensional global hybrid simulations with proton particles and fluid electrons. The ambient interplanetary magnetic field is perpendicular to the simulation plane. The results show the formation of a wake structure behind the obstacle with plasma depleted cavity in the center surrounded by low-frequency waves propagating away from the cavity. The properties and generating mechanism of these waves are discussed. We also study the dynamics of reflected protons and its influence on the lunar plasma environment. Different reflection models are compared with in-situ measurements of Japanese spacecraft SELENE (Kaguya).

Key words: lunar wake, hybrid simulations, magnetosonic waves.

Contents

1	Introduction	8
2	Basic tools and definitions	9
2.1	Definition of plasma	9
2.2	Plasma properties	10
2.3	Reference frames	12
2.4	Plasma dynamics	12
2.4.1	Single particle motion	13
2.4.2	Kinetic approach	14
2.4.3	Fluid approach	14
2.5	Solar wind	15
3	Lunar wake	17
3.1	Moon	17
3.2	Creation of the wake	17
3.3	In-situ observations	18
4	Numerical model	20
4.1	Description of the algorithm	20
4.2	Configuration of our simulations	24
5	Results and interpretations	27
5.1	Global plots	27
5.2	Fourier analysis	32
5.3	Reduced distribution functions	34
5.4	Reflected protons	36
5.5	Comparison with data from Kaguya	41
6	Conclusions	43
A	Constants and values	45

List of used symbols

B	magnetic field
B_{cav}, B_{sw}	magnitude of magnetic field in the cavity and in ambient solar wind
β_e, β_p	electron and proton beta
c	speed of light
$\delta\mathbf{B}$	fluctuations of magnetic field
E	electric field
e	electron (proton) charge
ϵ_0	vacuum permeability
k	wave vector
k	wave number
k_B	Boltzmann constant
λ_D	Debye length
Λ_p	proton inertial length
m_s	mass of specie s
μ_0	vacuum susceptibility
n_s	number density of specie s
Ω_p, ω_{pp}	proton plasma frequency
ω_{gp}	proton gyrofrequency
q_s	charge of specie s
r_{gs}	gyroradius of specie s
R_L	lunar radius
T_e, T_p	electron and proton temperature
$T_{\perp p}, T_{\parallel p}$	perpendicular and parallel proton temperature
v_{\perp}	speed in the plane perpendicular to B
v_A	Alfvén speed
v_s	speed of ion acoustic wave
\mathbf{v}_{sw}	solar wind bulk velocity
$v_{th s}$	thermal speed of specie s

Chapter 1

Introduction

The Moon has no atmosphere nor significant global dipolar magnetic field. Therefore the solar wind particles directly impact its surface forming a lunar wake structure on the nightside of the Moon. Studying the interaction between the solar wind and the Moon is important for understanding the lunar plasma environment. It has been believed that all particles hitting the Moon are absorbed by the lunar surface. But the in-situ measurements of the spacecraft SELENE (Kaguya) discovered that about one percent of solar wind protons is reflected and picked-up by the solar wind [18]. These protons were then detected in the deepest region of the near-Moon wake [16]. It shows that the simplified picture of the Moon as a passive absorber of the solar wind is incomplete.

The bombardment of the lunar surface by charged particles may also lead to charging and mobilization of lunar dust. The L-DEPP (Lunar Dust and Plasma Package) instrument onboard first ESA lunar lander will perform a comprehensive diagnosis of this dusty plasma environment.

We study the solar wind-Moon interaction by means of two-dimensional hybrid numerical simulations. We focus on periodical kinetic effects which are exhibited in the wake. Then we implement proton reflections on the lunar surface using two different reflection models. The influence of reflected protons on the global lunar plasma environment is discussed. Finally, we compare the results with real in-situ observations.

The thesis is organized as follows. First, in Chapter 2 we describe basic properties and behavior of plasma and solar wind. Chapter 3 is devoted to the description of the Moon and its interaction with the solar wind. Previous in-situ observations are summarized here. In Chapter 3 we present the numerical model used in the thesis and the particular simulation configurations. The main results are discussed in Chapter 4.

Chapter 2

Basic tools and definitions

Let us give the definition of a plasma, its properties, and several different approaches to the description of plasma dynamics.

2.1 Definition of plasma

There are many states of matter in nature. The most known are solids, liquids, and gases - the states of the things of our everyday lives. Some matters can change states during processes like melting, freezing, vaporization, condensation, sublimation, or deposition. These state changes can occur when pressures or temperatures are changed.

If a gas is warmed up to a temperature of several thousand degrees of Celsius, the molecules and atoms are shredded to ions and electrons. This process is called ionization and the new state of such a gas is called *plasma*. The inverse process is known as deionization. Thus, we can say that a plasma is a gas of charged particles, which consists of equal numbers of free positive and negative charge carriers [1].

Plasma has some interesting properties. Mainly, unlike gas, it may self-generate magnetic fields and electric currents, and respond strongly and collectively to electromagnetic forces. Since the particles that compose plasma carry electric charges, plasma can conduct electricity.

Every charged particle generates a microscopic electric field. Moving charges generate magnetic fields. The motion of charged particles is affected by these electromagnetic fields. Analyzing the development of any plasma system requires simultaneous solving of both field and particle motional equations. This is the basic difficulty of plasma behavior research.

In order for general ionized medium to behave like plasma, it must satisfy three main conditions.

Large dimensions. First of all, plasma behaves quasineutrally in the stationary state. It means that, on average, plasma looks electrically neutral to the outside. Any particle with charge q in free space generates the electric *Coulomb potential* field

$$\Phi_C = \frac{q}{4\pi\epsilon_0 r}. \quad (2.1)$$

In plasma, such an electric field is screened out by the Coulomb fields of the many other charged particles around. The Coulomb potential is then replaced by *Debye potential*

$$\Phi_D = \frac{q}{4\pi\epsilon_0 r} \exp\left(-\frac{r}{\lambda_D}\right). \quad (2.2)$$

The exponential function cuts off the potential at distances $r > \lambda_D$. This behavior is called *Debye shielding* effect. The characteristic length, λ_D , is called *Debye length*. The thermal energy of particles disturbs the electrical neutrality in plasma. On the other hand, any charge separation results in electrostatic potential energy, which tends to restore charge neutrality. Debye length is the distance, over which a balance between these two energies is obtained. In order for plasma to be quasineutral, the Debye length must be small enough compared to physical dimensions of the system, L ,

$$\lambda_D \ll L. \quad (2.3)$$

Sufficient amount of particles. The shielding effect is a result of particles collective behavior inside the *Debye sphere* of radius λ_D . Therefore it is necessary that this sphere contains enough particles. If we introduce the *plasma parameter* $\Lambda = n_e \lambda_D^3$, then this condition can be expressed as

$$\Lambda \gg 1. \quad (2.4)$$

Low amount of collisions. The third criterion for an ionized medium to behave as plasma is the low *collisions frequency* between particles, ν_C . In other words, the *Coulomb collision time*, $\tau_C = 1/\nu_C$, must be much longer than any other characteristic time of variation in the plasma. If the collisions occur too often, the particles are forced into equilibrium with each other and the medium behave rather like neutral gas. The most fundamental frequency in plasma is the *electron plasma frequency*, ω_{pe} . It gives the oscillation frequency of electrons columns against background plasma. The requirement of low collision frequency can be then written as

$$\tau_C \omega_{pe} \gg 1. \quad (2.5)$$

Such plasma is often called *collisionless*.

2.2 Plasma properties

We deal with classical non-relativistic plasma. It contains very large number of particles so that it is possible to define analogical quantities as in the case of neutral gas. The plasma consists of negatively charged electrons and positive ions. The quantities often describe the particular species (electrons, ions) separately. We will distinguish between species by different subscripts - e for electrons, i for ions, p for protons. Ordinary species will be subscripted by s .

The basic quantities describing plasma are: temperatures, T_s , number densities, n_s , ambient magnetic field, \mathbf{B} , and charges of particles in each specie, q_s . Other plasma parameters can be expressed as functions of these quantities. We also use some physical constants: Boltzmann constant, k_B , elementary charge, e , free space permittivity, ϵ_0 , free space permeability, μ_0 , and speed of light, c . The mass of a particle is denoted by m_s . The values of constants are listed in Appendix A.

The temperature, T_s , is considered as a kinetic temperature for the Maxwellian velocity distribution. It merely contains information about the average kinetic energy in plasma. Different particle species can have different temperatures. Also, when an external magnetic field is present, plasma can be anisotropic and the temperatures in direction perpendicular to the magnetic field, $T_{\perp s}$, and those in direction parallel to the magnetic field, $T_{\parallel s}$, are generally different. The pressure of plasma particles is simply associated with the temperature by

$$p_s = n_s k_B T_s. \quad (2.6)$$

We can define the thermal velocity by

$$v_{ths} = \left(\frac{k_B T_s}{m_s} \right)^{1/2}. \quad (2.7)$$

One of the most important parameter of plasma is the Debye length described in previous section

$$\lambda_D = \left(\frac{\epsilon_0 k_B T_e}{n_e e^2} \right)^{1/2}. \quad (2.8)$$

It grows with increasing temperature and decreasing density.

The most fundamental frequency of the plasma is the plasma frequency described in previous section

$$\omega_{ps} = \left(\frac{n_s q_s^2}{m_s \epsilon_0} \right)^{1/2}. \quad (2.9)$$

The total pressure is defined as a sum of thermal pressure (2.6) and magnetic pressure $B^2/2\mu_0$. It is spatially constant when the plasma is in equilibrium. Therefore we can define the ratio between thermal and magnetic pressure called *plasma beta*

$$\beta_s = \frac{n_s k_B T_s}{B^2/2\mu_0}. \quad (2.10)$$

The Alfvén speed is the fundamental speed at which magnetic signals can be transported through the plasma by waves. In other words, it is the typical speed to which the magnetic field can accelerate the plasma

$$v_A = \frac{B}{\sqrt{\mu_0 \rho}}, \quad (2.11)$$

where $\rho = \sum_s n_s m_s$ is the total mass density of the charged plasma particles.

2.3 Reference frames

Consider plasma moving with the non-relativistic bulk velocity \mathbf{v} with respect to the rest frame \mathcal{R} , where the magnetic and electric fields are respectively \mathbf{B} and \mathbf{E} . These fields are transformed to the plasma frame \mathcal{R}' by the Lorentz transformation as

$$\begin{aligned}\mathbf{E}' &= \mathbf{E} + \mathbf{v} \times \mathbf{B} \\ \mathbf{B}' &= \mathbf{B} - \mathbf{v} \times \mathbf{E}/c^2.\end{aligned}\tag{2.12}$$

We neglect terms of order v^2/c^2 . Since plasma is quasineutral on large-scales, the electric field nearly vanishes in the plasma frame, $\mathbf{E}' = 0$. Thus, we get from (2.12)

$$\begin{aligned}\mathbf{E} &= -\mathbf{v} \times \mathbf{B} \\ \mathbf{B} &= \mathbf{B}' + \mathbf{v} \times \mathbf{E}/c^2 = \mathbf{B}' - \mathbf{v} \times (\mathbf{v} \times \mathbf{B})/c^2 \simeq \mathbf{B}'.\end{aligned}\tag{2.13}$$

Hence the magnetic field is independent of the reference frame, whereas the electric field depends strongly on the referenece frame. The electric field in (2.13) is called *motional electric field*.

2.4 Plasma dynamics

Plasma consists of large number of charged particles which interact with each other through electromagnetic forces. In other words, the charges generate electric field, while the moving charged particles are the sources of magnetic field. This relation between fields and particles is described by *Maxwell's equations*

$$\begin{aligned}\nabla \times \mathbf{B} &= \mu_0 \mathbf{j} + \epsilon_0 \mu_0 \frac{\partial \mathbf{E}}{\partial t} \\ \nabla \times \mathbf{E} &= -\frac{\partial \mathbf{B}}{\partial t} \\ \nabla \cdot \mathbf{B} &= 0 \\ \nabla \cdot \mathbf{E} &= \rho/\epsilon_0\end{aligned}\tag{2.14}$$

where ρ is the charge density, \mathbf{j} is the electric current density, and ϵ_0 and μ_0 are the vacuum permittivity and susceptibility, respectively (see Appendix A). On the other hand, the motion of charged particles is strongly influenced by electromagnetic fields. The electric field, \mathbf{E} , acts upon every charged particle by the *Coulomb force*

$$\mathbf{F}_C = q\mathbf{E}\tag{2.15}$$

The magnetic field, \mathbf{B} , is the origin of the *Lorentz force*

$$\mathbf{F}_L = q(\mathbf{v} \times \mathbf{B})\tag{2.16}$$

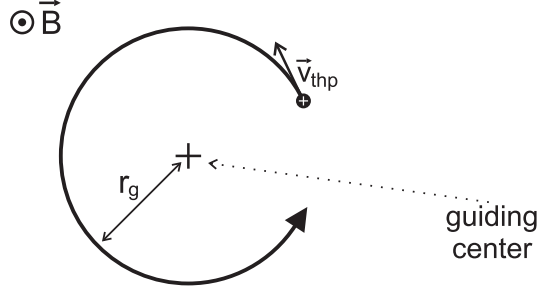


Figure 2.1: Gyration of the proton in a uniform static magnetic field.

Thus, the equation of motion of charged particle with mass m in electromagnetic field can be written according to equations (2.15) and (2.16) as

$$m \frac{dv}{dt} = q(\mathbf{E} + \mathbf{v} \times \mathbf{B}) \quad (2.17)$$

In order to describe the dynamics of plasma, we have to solve Maxwell's equations (2.14) and the equation of motion (2.17) for each particle simultaneously. Such a solution is too difficult, since the electric and magnetic fields appearing in every particle equation of motion include the internal fields generated by every other particle. In fact, we are interested in averaging quantities like density, pressure, and temperature rather than the position and velocity of each individual particle. Therefore, we use some approximations for description of plasma dynamics. In following sections, three basic approaches are described.

2.4.1 Single particle motion

Single particle motion description is the simplest approach. It describes the motion of one charged particle in prescribed external electric and magnetic fields. It is useful to study the motion of individual particle, but it neglects the collect behavior of plasma. Nevertheless, this approach enables us to understand fundamental effects in plasma related to *gyration*.

Let us consider a motion of a charged particle in a uniform magnetostatic field along the z axis (see figure 2.1). Since there is no electric field, the equation of motion (2.17) reduces to

$$m \frac{dv}{dt} = q(\mathbf{v} \times \mathbf{B}), \quad (2.18)$$

where $\mathbf{B} = (0, 0, B)$. If the velocity vector lies in the plane perpendicular to \mathbf{B} , the solution of (2.18) is a circular motion (gyration) in this plane with the frequency

$$\Omega_s = \omega_{gs} = \frac{q_s B}{m_s} \quad (2.19)$$

called *cyclotron frequency* or *gyrofrequency*. The radius of the orbit

$$r_{gs} = \frac{v_{\perp}}{|\omega_{gs}|} = \frac{m_s v_{\perp}}{|q_s| B} \quad (2.20)$$

is called *Larmor radius* or *gyroradius*. Here v_{\perp} denotes the constant speed in the plane perpendicular to \mathbf{B} . Whenever the particle has a non-zero velocity parallel to the magnetic field, the actual trajectory of the particle is three-dimensional and looks like a helix. In plasma, the role of v_{\perp} is played by thermal speed (2.7).

2.4.2 Kinetic approach

The basis of kinetic approach is the six-dimensional *phase space* with coordinate axes (\mathbf{x}, \mathbf{v}) . A particle at a certain time is represented as one point in this space. In phase space, a *distribution function* $f_s(\mathbf{x}, \mathbf{v}, t)$ for each specie s can be defined. It represents a probability of a particle to be found in phase space volume element $d\mathbf{x}d\mathbf{v}$.

For collisionless plasma we can derive the evolution equation of the distribution function in phase space

$$\frac{\partial f_s}{\partial t} + \mathbf{v} \cdot \nabla_{\mathbf{x}} f_s + \frac{q_s}{m_s} (\mathbf{E} + \mathbf{v} \times \mathbf{B}) \cdot \nabla_{\mathbf{v}} f_s = 0 \quad (2.21)$$

called *Vlasov equation*. Here the indices of two ∇ operators indicate differentiation with respect to particle position and velocity. This equation is coupled through the last term to the full set of Maxwell's equations (2.14), where the charge and current densities can be expressed by

$$\rho = \sum_s q_s \int f_s d^3v$$

$$\mathbf{j} = \sum_s q_s \int f_s \mathbf{v} d^3v$$

The distribution function permits to calculate macroscopic variables by simple integrations:

$$n = \int f(\mathbf{v}) d^3v \quad (\textit{number density})$$

$$\mathbf{v}_b = \frac{1}{n} \int \mathbf{v} f(\mathbf{v}) d^3v \quad (\textit{bulk flow velocity})$$

$$\mathbf{P} = m \int (\mathbf{v} - \mathbf{v}_b)(\mathbf{v} - \mathbf{v}_b) f(\mathbf{v}) d^3v \quad (\textit{pressure tensor})$$

$$T = \frac{m}{3k_B n} \int (\mathbf{v} - \mathbf{v}_b) \cdot (\mathbf{v} - \mathbf{v}_b) f(\mathbf{v}) d^3v \quad (\textit{kinetic temperature})$$

2.4.3 Fluid approach

In many cases, it is not necessary to know the exact evolution of the distribution function. It is often sufficient to determine the development of the moments of $f(\mathbf{x}, \mathbf{v}, t)$ given above.

The *multi-fluid* plasma picture offers a general description where individual ion species and electrons are described separately. The fundamental equations of multi-fluid theory can

	protons	electrons
mass m	$1.67 \cdot 10^{-27}$ kg	$9.11 \cdot 10^{-31}$ kg
temperature T	$1.2 \cdot 10^5$ K	$1.4 \cdot 10^5$ K
thermal velocity v_{th}	35 km/s	1500 km/s
gyro-frequency ω_g	0.5 s ⁻¹	880 s ⁻¹
gyro-radius r_g	65 km	1.7 km
plasma frequency ω_p	$3 \cdot 10^{-3}$ s ⁻¹	0.1 s ⁻¹

Table 2.1: Comparison of the solar wind species close to the Earth.

be obtained by integration of the Vlasov equation (2.21)

$$\frac{\partial n_s}{\partial t} + \nabla \cdot (n_s \mathbf{v}_s) = 0 \quad (\text{continuity equation})$$

$$\frac{\partial(n_s \mathbf{v}_s)}{\partial t} + \nabla \cdot (n_s \mathbf{v}_s \mathbf{v}_s) = -\frac{1}{m_s} \nabla \cdot \mathbf{P}_s + \frac{n_s q_s}{m_s} (\mathbf{E} + \mathbf{v}_s \times \mathbf{B}) \quad (\text{equation of motion})$$

which must be completed with equations of state and with Maxwell's equations (2.14).

The simpler fluid model is called *magnetohydrodynamics*. It treats the plasma as a single fluid governed by a combination of Maxwell's equations (2.14) and following set of equations

$$\frac{\partial n}{\partial t} + \nabla \cdot (n \mathbf{v}) = 0 \quad (\text{continuity equation})$$

$$\frac{\partial(nm\mathbf{v})}{\partial t} + \nabla \cdot (nm\mathbf{v}\mathbf{v}) = -\nabla \cdot \mathbf{P} + \rho\mathbf{E} + \mathbf{j} \times \mathbf{B} \quad (\text{equation of motion})$$

$$\mathbf{E} + \mathbf{v} \times \mathbf{B} = \eta \mathbf{j} + \frac{1}{ne} \mathbf{j} \times \mathbf{B} - \frac{1}{ne} \nabla \cdot \mathbf{P}_e + \frac{m_e}{ne^2} \frac{\partial \mathbf{j}}{\partial t} \quad (\text{Ohm's law})$$

2.5 Solar wind

The Sun continually ejects one million tonnes of a mass into interplanetary space per second. This mass is called solar wind and it consists of electrons, protons, and a small admixture (about 5%) of alpha-particles. The amount of alpha-particles is so small that their presence is often neglected, so as throughout this thesis. The solar wind originates in solar atmosphere and is accelerated in solar corona to the velocity of 300–1400 km/s (cf [13]). At the beginning (in the solar corona) the solar wind has a temperature of about $1.6 \cdot 10^6$ K and a density of about $5 \cdot 10^{17}$ cm⁻³. Then the solar wind propagates away from the Sun and during that it is diluted and cooled down.

Close to the Earth, the temperatures of protons and electrons decrease to the values of about $T_i = 1.2 \cdot 10^5$ K and $T_e = 1.4 \cdot 10^5$ K, respectively (cf [13]). Whereas the difference between temperatures is not too big, electrons and protons differ considerably in thermal velocity. The thermal velocity of protons is lower than the streaming velocity of solar wind, but the thermal velocity of electrons is higher than the bulk velocity. The comparison of the

density n	5 cm^{-3}
SW velocity v_{sw}	250 km/s
magnetic field B	5 nT
Debye length λ_D	10 m
Alfvén velocity v_A	50 km/s
plasma beta β	1

Table 2.2: Solar wind parameters close to the Earth.

most important physical parameters of both species of the solar wind are presented in Table 2.1.

The mean free path of solar wind particles close to the Earth is about 1 AU so that the solar wind here is considered as a collisionless fully ionized plasma of the total density of about 5 cm^{-3} . One of the most important properties of the solar wind is its magnetization. The magnetic field produced by the Sun is frozen in solar wind due to its high conductivity. The strength of the magnetic field at the distance of 1 AU from the Sun is about 5 nT. The plasma beta is approximately equal to one, *i. e.*, the plasma and magnetic pressure are roughly equal in the solar wind.

Chapter 3

Lunar wake

3.1 Moon

The Moon is our only natural satellite and it is the fifth largest satellite in the solar system. It has been the first (and up to now the only) object in the space people have landed on. The Moon orbits the Earth at the distance of 363,104 km (perigee) up to 405,696 km (apogee). It makes a complete orbit around the Earth with respect to the fixed stars about once every 27.32 days (its sidereal period). It is in synchronous rotation with the Earth (rotation period 27.32 days), always showing the same face.

3.2 Creation of the wake

Since, unlike the Earth, the Moon has almost no atmosphere nor significant global dipolar magnetic field, solar wind particles directly impact its surface. First observations showed that the Moon behaves like a non-conducting dielectric sphere, which absorbs all hitting particles. Thus, a plasma-depleted cavity is formed behind the Moon along the solar wind flow, which is called *lunar wake*.

So what happens downstream of the Moon? Let us first neglect the magnetic field. Since the thermal velocity of electrons is much higher than the bulk speed of solar wind (see Table 2.1), they tend to fill the wake, but the protons cannot do so easily. In the solar wind frame, the Moon moves with the velocity $-\mathbf{v}_{sw}$, whereas the plasma moves sideways with the speed $\sim v_{thp} \ll v_{sw}$ to fill the cavity. It creates a cone-like region of depleted plasma of the length $\sim R_L v_{sw}/v_{thp}$. Since the electrons fill the wake faster than protons, they produce inward electric field, which has two effects. First, it curves the paths of protons and accelerates them towards the axis. Second, the depletion of protons creates a negative space charge, which repels the electrons.

The magnetic field changes this simplified picture. The orientation of the field is very important as shown in Figure 3.1. In case *a*, the particles can still diffuse to the cavity and the shape does not differ significantly from the case without the magnetic field. As the angle

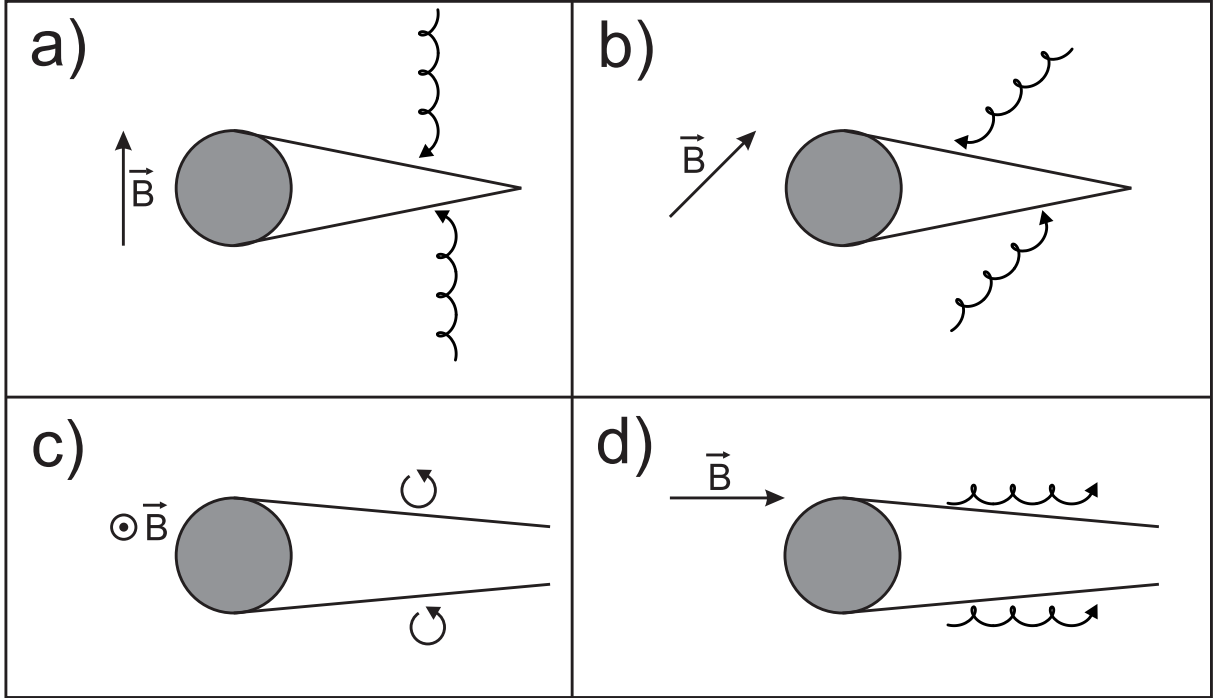


Figure 3.1: Examples of interplanetary magnetic field configuration. In cases *a* and *b*, protons can simply move along field lines to fill the wake. If the magnetic field is perpendicular to the plane (*c*) or parallel to the wake axis (*d*), the protons cannot fill the cavity by moving along field lines. Hence the plasma-depleted cavity is of larger size.

between the solar wind velocity and ambient magnetic field get smaller (Figure 3.1 b, d), the cavity is of larger size, because the particles must overcome longer distances to get the center of the cavity along field lines. The case *c* is valid only from two-dimensional point of view. This is the case we will deal with in the thesis.

3.3 In-situ observations

The beginning of the research of lunar plasma environment is, naturally, associated with first flights of space satellites. First in-situ data from the lunar wake were based on the measurements made by Explorer 35 through the years 1967 – 1973 [14]. Also the Apollo surface and orbital experiments [19] made some measurements of the lunar wake, but, as in the case of Explorer 35, with a very low resolution. However, all these experiments were able to detect a significant depletion of solar wind density behind the Moon.

Then several decades passed with relatively little interest in lunar research. On December 27, 1994, the WIND spacecraft used the Moon for a gravitational assist. It passed at a distance of 6.5 lunar radii through the lunar wake and made several measurements in this area with all its instruments switched on. The data showed a number of interesting plasma

physical processes. They were described in many papers published mostly in 1996 [3, 4, 11, 17]. Several numerical simulations were performed to explain observed phenomena [2, 5, 10, 21].

A systematical research of the lunar plasma environment started in 2007 by Japanese spacecraft SELENE (Kaguya) [15, 16, 18] followed by Indian spacecraft Chandrayaan-1 [7, 22]. Their measurements have indicated that the simplified picture of the Moon as a passive solar wind absorber is incomplete. The instruments onboard these spacecrafts detected solar wind ions reflected on the lunar dayside surface. These ions were also detected inside the lunar near wake. Let us note that Apollo 12 and 14 experiments observed energetic ion fluxes at the nightside surface [6].

Chapter 4

Numerical model

In principle, there are following main types of plasma numerical models:

- **kinetic model** - ions and electrons are described as individual particles
- **fluid model** - ions and electrons are described as fluids
- **hybrid model** - ions are considered particles whereas electrons are modeled as a fluid

Due to the small electron gyroradius and high electron gyrofrequency compared with corresponding proton values (Table 2.1), the kinetic model requires higher spatial and temporal resolutions. Therefore the simulation size and time are very limited and thus this model is unusable for our purposes. On the other hand, fluid models enable large simulation domains and long times, but the resolutions are so small that the kinetic effects related to the gyroradius become neglected.

Hybrid models represent the combination of the kinetic and fluid approach. Ions are modeled as separate particles whereas electrons are considered as an electroneutralising massless fluid. In fact, describing the motion of each real particle would be very time and memory consuming. Therefore a concept of so called *macroparticles* (or *superparticles*) is introduced. Each macroparticle represents the mass center of a real particles cloud.

4.1 Description of the algorithm

In our simulations, we use a hybrid model called *Current Advance Method and Cyclic Leapfrog algorithm* (CAM-CL). It was described in [12]. Although the algorithm is independent of dimension number, we will explain it from two-dimensional point of view. The extension to three dimensions is straightforward.

The algorithm is modeled by *Particle In Cell scheme* (PIC). Each ion superparticle is described by five real numbers: two for the position and three for velocity coordinates. The simulation domain is divided into $N_x \times N_y$ cells. They form a rectangular grid, called *magnetic field grid*. The nodes of this grid have integer indices, at which magnetic field \mathbf{B} ,

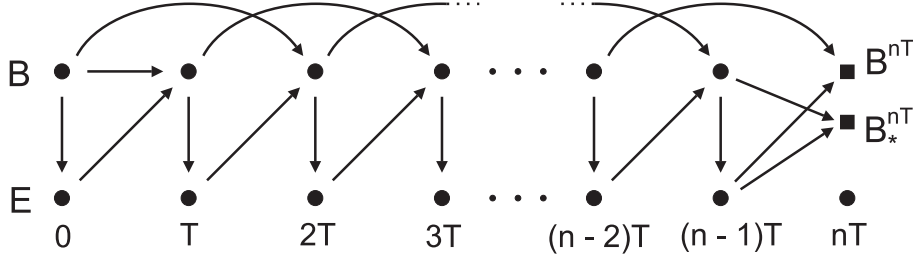


Figure 4.1: The scheme of the cyclic leapfrog algorithm.

charge density ρ , current densities \mathbf{J}_s , and electron pressure p_e are computed. Electric field \mathbf{E} has its own grid which is shifted by half-cell in both directions so that the nodes of *electric field grid* lie in centers of cells of magnetic field grid.

Following equations are used for plasma development:

$$\mathbf{E} = \frac{1}{\rho} \left(\frac{(\nabla \times \mathbf{B}) \times \mathbf{B}}{\mu_0} - \mathbf{J} \times \mathbf{B} - \nabla p_e \right) + \eta(\nabla \times \mathbf{B}) \quad (\text{Ohm's law}) \quad (4.1)$$

$$\frac{\partial \mathbf{B}}{\partial t} = -\nabla \times \mathbf{E} \quad (\text{Faraday's law}) \quad (4.2)$$

$$\frac{d\mathbf{v}}{dt} = \frac{q_s}{m_s} (\mathbf{E} + \mathbf{v}_s \times \mathbf{B}) \quad (\text{Newton's law}) \quad (4.3)$$

Here $\rho = \sum_s n_s q_s$ denotes the ionic charge density, $\mathbf{J} = \sum_s \mathbf{J}_s$ stands for the ionic current density, η is a resistivity term. The electron pressure is given by relation $p_e = n_e k_B T_e$. Note that the electron temperature T_e is considered to be constant. In order for plasma to be quasineutral, we compute the concentration of electrons from the total ionic charge density

$$n_e = \frac{\rho}{e}. \quad (4.4)$$

The spacial derivatives transform quantities between electric and magnetic field grids. An example of derivative computing is sketched in Figure 4.2. The derivative in some node in the right grid is computed from four nearest nodes in the left grid

$$\frac{\partial g}{\partial x}(i + 1/2, j + 1/2) = \frac{1}{2\Delta x} (g(i + 1, j) + g(i + 1, j + 1) - g(i, j) - g(i, j + 1)) \quad (4.5)$$

The moments ρ and \mathbf{J} are evaluated in grid nodes. Each particle located in some cell contributes to this moments computed at cell corners with certain weights depending on its position in the cell (see Figure 4.3).

Let us describe one step of CAM-CL algorithm, *i.e.*, the development of the plasma from time $t = t_0$ to $t = t_0 + \Delta t$. We use notation $g^n = g(t + n\Delta t)$ and $G^{mn} = G(\mathbf{x}^m, \mathbf{v}^n)$. Expressions of the form $E = E(\rho, \mathbf{J}, \mathbf{B})$ represents the computation of electric field by Ohm's law (4.1). Assume that at the beginning of each cycle, we know $\mathbf{x}^{1/2}$, \mathbf{v}^0 , \mathbf{B}^0 . Also the moments ρ^0 , $\rho^{1/2}$, \mathbf{J}^0 , and $\mathbf{J}^{1/2}$ are known. Each simulation step can be divided into following phases:

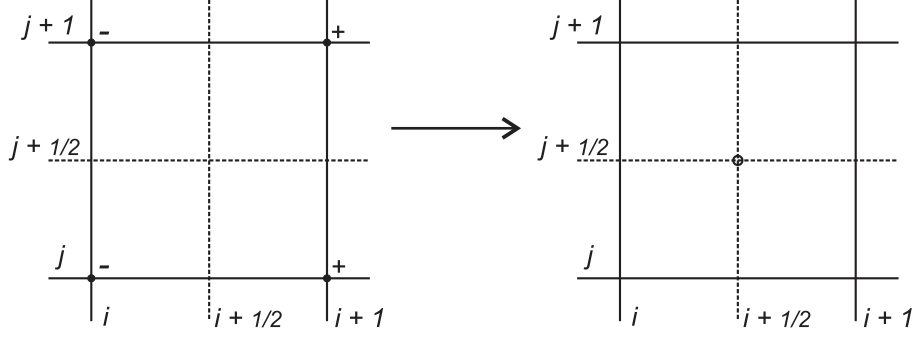


Figure 4.2: An example of derivative evaluation. Here the derivative $\partial/\partial x$ transforms a quantity from the magnetic field grid (left) to the electric field grid (right).

1. Advancing the magnetic field. The magnetic field \mathbf{B} is advanced half-time step forward using cyclic leapfrog (CL) algorithm. Integration of Faraday's law (4.2) yields

$$\mathbf{B}^{1/2} = \mathbf{B}^0 + \int_0^{\Delta t/2} \nabla \times \mathbf{E}(\rho^0, \mathbf{J}^{0\ 0}, \mathbf{B}(t)) dt. \quad (4.6)$$

The magnetic field usually requires a smaller time step than the particles to resolve its evolution. Therefore we use n substeps for magnetic field update half-step $\Delta t/2$ forward. The CL algorithm is sketched in Figure 4.1. The upper part of the scheme reveals the origin of the name *cyclic leapfrog*. If we denote $T = \frac{\Delta t}{2n}$, the CL algorithm can be written as

$$\begin{aligned} \mathbf{E}^0 &= \mathbf{E}(\rho^0, \mathbf{J}^{0\ 0}, \mathbf{B}^0) \\ \mathbf{B}^T &= \mathbf{B}^0 - T \nabla \times \mathbf{E}^0 \\ \mathbf{E}^T &= \mathbf{E}(\rho^0, \mathbf{J}^{0\ 0}, \mathbf{B}^T) \\ \mathbf{B}^{2T} &= \mathbf{B}^0 - 2T \nabla \times \mathbf{E}^T \\ \mathbf{E}^{2T} &= \mathbf{E}(\rho^0, \mathbf{J}^{0\ 0}, \mathbf{B}^{2T}) \\ \mathbf{B}^{3T} &= \mathbf{B}^T - 2T \nabla \times \mathbf{E}^{2T} \\ &\vdots \\ \mathbf{E}^{(n-2)T} &= \mathbf{E}(\rho^0, \mathbf{J}^{0\ 0}, \mathbf{B}^{(n-2)T}) \\ \mathbf{B}^{(n-1)T} &= \mathbf{B}^{(n-2)T} - 2T \nabla \times \mathbf{E}^{(n-2)T} \\ \mathbf{E}^{(n-1)T} &= \mathbf{E}(\rho^0, \mathbf{J}^{0\ 0}, \mathbf{B}^{(n-1)T}) \\ \mathbf{B}^{nT} &= \mathbf{B}^{(n-2)T} - 2T \nabla \times \mathbf{E}^{(n-1)T} \\ \mathbf{B}_*^{nT} &= \mathbf{B}^{(n-1)T} - T \nabla \times \mathbf{E}^{(n-1)T} \\ \mathbf{B}^{1/2} &= \frac{1}{2} (\mathbf{B}^{nT} + \mathbf{B}_*^{nT}) \end{aligned}$$

Note that we use 10 substeps in our simulations. Finally, we get the electric field, which will be used only for the advancement of the current in next step.

$$\mathbf{E}^* = \mathbf{E}(\rho^{1/2}, \mathbf{J}^{1/2\ 0}, \mathbf{B}^{1/2}). \quad (4.7)$$

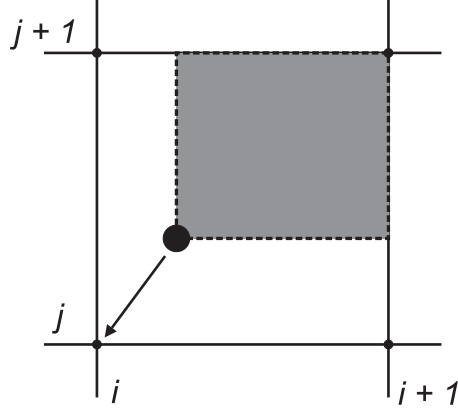


Figure 4.3: A superparticle in a simulation cell. The gray area represents the weight of particle contribution to the node at (i, j) .

2. Advancing the ionic current density. From Newton's law (4.3) we can obtain a momentum conservation equation for ions

$$\frac{d\mathbf{J}_i}{dt} = \sum_s \frac{q_s}{m_s} (n_s q_s \mathbf{E} + \mathbf{J}_s \times \mathbf{B}). \quad (4.8)$$

By its integration we can advance the ionic current

$$\mathbf{J}^{1/2 \ 1/2} = \mathbf{J}^{1/2 \ 0} + \frac{\Delta t}{2} (\rho_r^{1/2} \mathbf{E}^* + \mathbf{J}_r^{1/2 \ 0} \times \mathbf{B}^{1/2}). \quad (4.9)$$

The quantities $\rho_r^{1/2}$ and $\mathbf{J}_r^{1/2 \ 0}$ are defined by

$$\begin{aligned} \rho_r^{1/2} &= \sum_s r_s q_s n_s^{1/2} \\ \mathbf{J}_r^{1/2 \ 0} &= \sum_s r_s \mathbf{J}_s^{1/2 \ 0} \end{aligned}$$

where $r_s = q_s/m_s$ is the charge to mass ratio of the ionic specie s .

3. Pushing the superparticles. We are now ready to push superparticles. First, we update the electric field using the advanced current

$$\mathbf{E}^{1/2} = \mathbf{E}(\rho^{1/2}, \mathbf{J}^{1/2 \ 1/2}, \mathbf{B}^{1/2}). \quad (4.10)$$

Now we push the particles using mid-point method for the advancement of velocities

$$\begin{aligned} \mathbf{v}^{1/2} &= \mathbf{v}^0 + \frac{\Delta t}{2} \frac{q}{m} (\mathbf{E}^{1/2} + \mathbf{v}^0 \times \mathbf{B}^{1/2}) \\ \mathbf{v}^1 &= \mathbf{v}^0 + \Delta t \frac{q}{m} (\mathbf{E}^{1/2} + \mathbf{v}^{1/2} \times \mathbf{B}^{1/2}) \\ \mathbf{x}^{3/2} &= \mathbf{x}^{1/2} + \mathbf{v}^1 \Delta t \end{aligned}$$

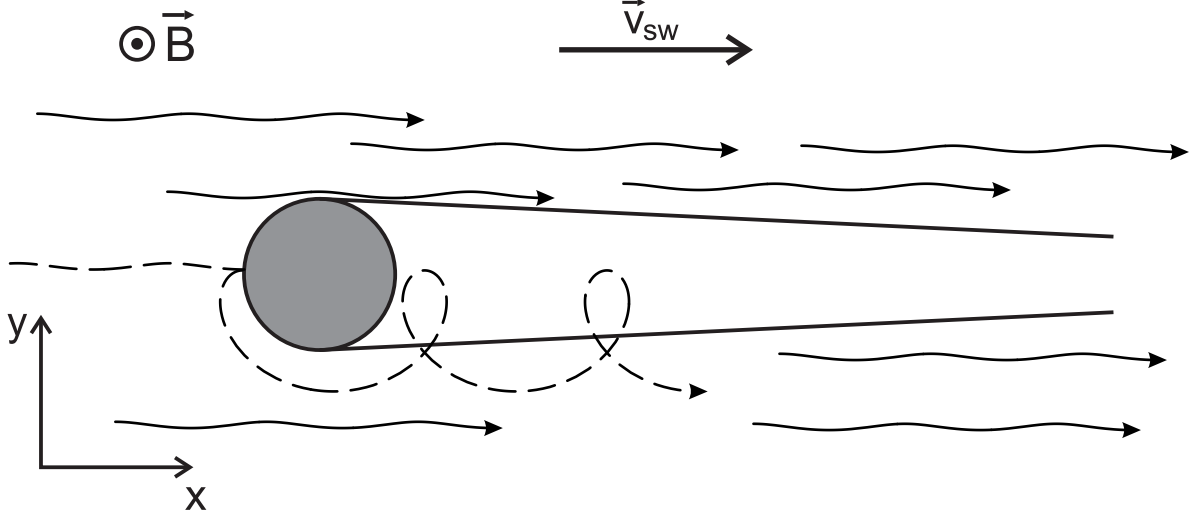


Figure 4.4: Sketch of the situation. Ambient magnetic field is perpendicular to the simulation plane. Examples of proton trajectories including a reflected proton (dashed line) are plotted.

During the advancement of superparticles we collect the moments $\rho^{3/2}$, $\mathbf{J}^{1/2 \ 1}$, and $\mathbf{J}^{3/2 \ 1}$. Then we calculate

$$\begin{aligned}\rho^1 &= \frac{1}{2} (\rho^{1/2} + \rho^{3/2}) \\ \mathbf{J}^{1 \ 1} &= \frac{1}{2} (\mathbf{J}^{1/2 \ 1} + \mathbf{J}^{3/2 \ 1})\end{aligned}$$

4. Advancing the magnetic field. Finally, the magnetic field is advanced again by second use of cyclic leapfrog algorithm

$$\mathbf{B}^1 = \mathbf{B}^{1/2} + \int_{\Delta t/2}^{\Delta t} \nabla \times \mathbf{E} (\rho^1, \mathbf{J}^{1 \ 1}, \mathbf{B}(t)) dt. \quad (4.11)$$

4.2 Configuration of our simulations

We have performed four simulations with different conditions. A 2.5-D version of the hybrid code is used. It has 2 spatial dimensions and 3 velocity dimensions. We use selenocentric coordinate system in the simulation X - Y plane, where the x-axis points tailward. The situation is sketched in Figure 4.4.

At the beginning of the simulation, the Moon represented by a disk of radius R_L is surrounded by isotropic Maxwellian protons with the constant solar wind speed $v_{sw} = 5v_A$. The initial ambient magnetic field is also introduced in the simulation plane. It is scaled to one, and its orientation differs in different simulation runs. Since the electric field is proportional to the factor $1/\rho$, we must avoid the plasma density dropping out below the value $n_{min} = 0.05$. Therefore, we start the simulation with some plasma superparticles

Simulation run	Ambient magnetic field	Reflection model
<i>a</i>	$\mathbf{B} = (\sqrt{2}/2, \sqrt{2}/2, 0)$	no reflections
<i>b</i>	$\mathbf{B} = (0, 0, 1)$	no reflections
<i>c</i>	$\mathbf{B} = (0, 0, 1)$	specular
<i>d</i>	$\mathbf{B} = (0, 0, 1)$	inverting

Table 4.1: List of performed simulations.

distributed also inside the obstacle. We use periodic boundary conditions at the borders of the simulation box.

The simulation units are derived from the properties of unperturbed plasma. The time is given in inversed proton gyrofrequency, $\Omega_p^{-1} = \omega_{gp}^{-1}$. The unit of space distances is proton inertial length, $\Lambda_p = c/\omega_{pp}$. It follows that the velocities are scaled by the Alfvén velocity v_A . The values of protonic and electronic betas are chosen to be $\beta_p = \beta_e = 1$.

We use spatial resolutions $\Delta x = \Delta y = 0.2\Lambda_p$ and the temporal resolution $\Delta t = 0.01\Omega_p^{-1}$. For calculations of electromagnetic fields we use substepping $\Delta t_B = \Delta t/10$. The simulation plane contains $N_x = 3200$ meshpoints in x-direction and $N_y = 2100$ meshpoints in y-direction. We use 200 superparticles per cell. Total simulation time is $t_{tot} = 90\Omega_p^{-1}$. Since the proton gyroradius $r_{gp} = 2\sqrt{\beta_p/\pi}\Lambda_p = 1.13\Lambda_p$, the selected space resolution $0.2\Lambda_p$ is sufficient to exhibit effects of proton gyromotion. Assuming the density $n_p = 5cm^{-3}$, the proton inertial length is $\Lambda_p = 102$ km. Since the Moon radius is 1738 km, we can set $R_L = 17\Lambda_p$. Note that it is possible to model the solar wind-Moon interaction on real scales. This is not true for example in Mercury simulations [20], where the ratio between the planet radius and λ_p is much higher and scaling down of the sizes is needed. The total sizes of our simulation box are $L_x = 38R_L$ and $L_y = 25R_L$.

Up to here, the simulation parameters are the same for all configurations. The list of performed simulations is given in Table 4.1. We denote different simulation runs by letters *a*, *b*, *c*, and *d*. They differ in the orientation of the ambient magnetic field and in the behavior of proton superparticles that hit the lunar surface.

In simulation *a* the vectors of the ambient magnetic field \mathbf{B} lie in the simulation plane ($\mathbf{B} = (\sqrt{2}/2, \sqrt{2}/2, 0)$). Thus the angle between \mathbf{B} and solar wind velocity v_{sw} is 45° . Such configuration was widely investigated [21] and we present it in this thesis only in the reason of comparison. All other simulations (*b*, *c*, and *d*) have been performed with the ambient magnetic field perpendicular to the X - Y plane, *i. e.*, $\mathbf{B} = (0, 0, 1)$.

When the superparticle in simulations *a* or *b* hit the lunar surface, it is removed from the simulation. In fact, it is removed with the probability $1 - n_{min} = 0.95$ in order to avoid very low plasma densities resulting to singularities of the electric field, as discussed above. Simulations *c* and *d* are extended by implementation of proton reflections. Thus, when the superparticle hit the surface of the Moon, it is reflected with the probability $f_R = 0.01$. We assume no velocity loss during reflection. The proportion of particles not removed from the

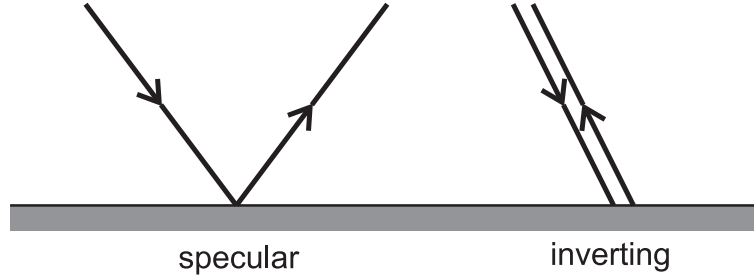


Figure 4.5: Illustrations of the two different reflection models used in simulations.

simulation remains unchanged, *i. e.*, $n_{min} = 0.05$.

The dependence of reflection angle on the incidence angle is still unknown. Moreover, since it probably depends on the microstructure of the lunar surface, it can also vary in time. We use two extremal reflection models (Figure 4.5).

Simulation *c* use a *specular* model, which assumes the Moon to be an ideal sphere. The incidence and reflection angle are equal in this case. Another model, which we have called *inverting*, is used in simulation *d*. The superparticle hitting the surface changes the sign of all velocity components. This model corresponds to very uneven surface.

The simulations were computed on 224 parallel nodes of *Amalka Supercomputing Facility* at the Academy of Sciences of the Czech Republic. The *MPI protocol* is used. The simulation plane is divided into $224 = 16 \times 14$ subdomains, each computed by one node.

Chapter 5

Results and interpretations

In this chapter we present the results from all performed simulations described above. We discuss the influence of the ambient magnetic field orientation and of the reflection model on the global behavior of plasma. Global distributions of some physical quantities are plotted. We make a Fourier analysis of magnetic field fluctuations in order to find properties of rarefaction waves. Several reduced distribution functions are also presented.

Then we focus on reflected protons. We explain the process of proton energization by self pick-up mechanism. We show examples of reflected protons trajectories and the dependence of proton destination on the reflection angle and impact position on the lunar surface. The consequences of using different reflection models are also discussed. Finally, we compare the simulation data with real in-situ observations of Japanese spacecraft SELENE.

5.1 Global plots

We present global plots of several plasma quantities as functions of x and y . For better comparison, each figure is divided into four panels in order to show one quantity for different simulation configurations side by side.

Upper two panels always correspond to the simulations without implementation of proton reflections on the lunar surface. They differ in the orientation of the ambient magnetic field. The left one is the only panel in the figure where the magnetic field vectors lie in the simulation plane, $\mathbf{B} = (\sqrt{2}/2, \sqrt{2}/2, 0)$. Other panels show the results of simulations with the magnetic field perpendicular to the simulation domain, $\mathbf{B} = (0, 0, 1)$. Bottom panels represent the simulations with one percent proton reflections with specular (left panel) and inverting (right panel) reflection model.

Let us start with the distribution of the proton **density** (Figure 5.1). In all cases, we see a vacuum region formed on the nightside of the Moon. It is surrounded by waves propagating away from the center and forming edges of lunar tail structure. At both edges of the tail, large rarefied plasma regions are observed.

Although the overall structure of the lunar wake is similar in all configurations, the

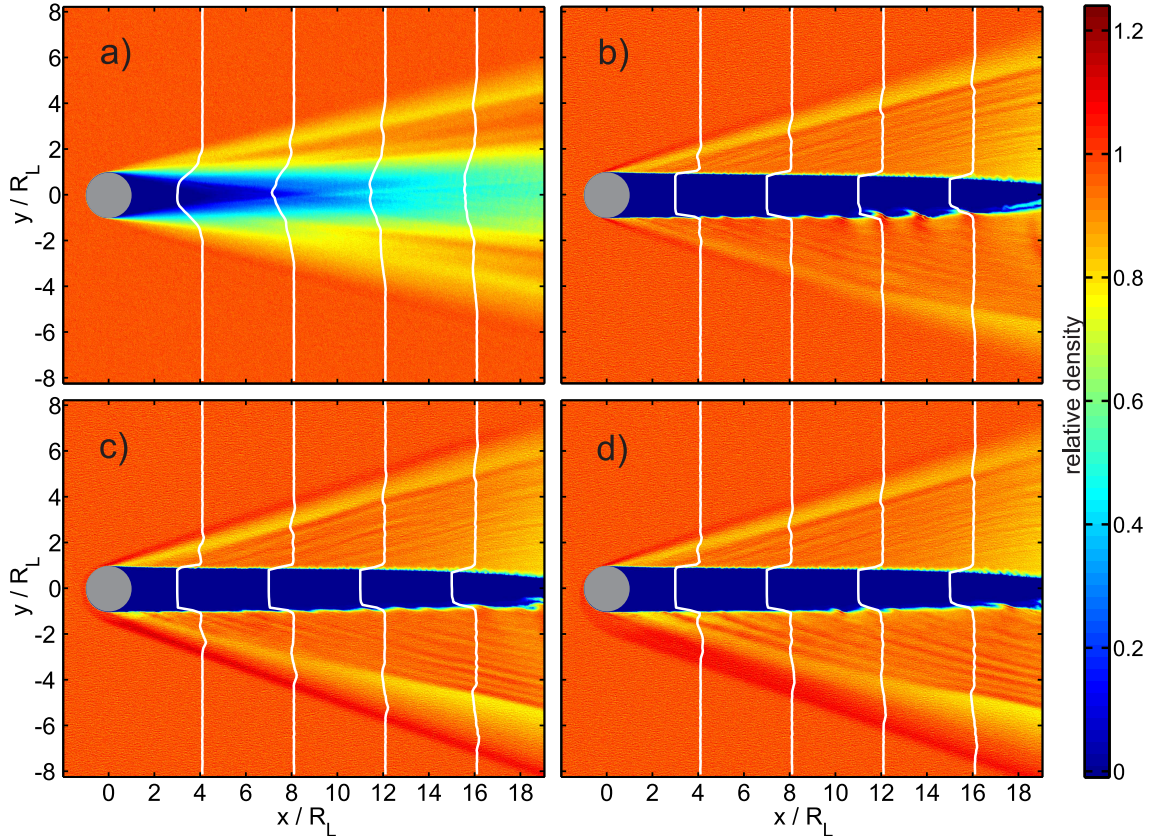


Figure 5.1: Proton density plots for various simulation runs: Panel *a* represents the case with ambient magnetic field vectors lying in the simulation plane (i.e. initially $B_z = 0$). Other panels show the situation with ambient magnetic field vectors perpendicular to the simulation plane (i.e. initially $B_x = B_y = 0$) and different reflection models: without reflection (*b*), specular (*c*), and inverting (*d*). Right panel shows the corresponding scale. Overlaid curves denote several profiles of the density in arbitrary units.

influence of the ambient magnetic field orientation on the lunar wake environment is crucial. In case *a*, plasma refills the cavity along magnetic field lines. Moreover, the gradient of the electronic pressure forms the ambipolar inward electric field at the cavity edges and this field accelerates the protons toward the wake center. Thus, the cavity is refilled relatively fast.

When the ambient magnetic field is perpendicular to the simulation plane (cases *b*, *c*, and *d*), the situation is absolutely different. The plasma particles cannot so easily move across magnetic field lines and the plasma-depleted cavity is of larger size as compared with the previous case (Figure 5.1 b - d). The waves propagating away from the cavity will be discussed in separate Section 5.2.

Introduction of proton reflections on the lunar surface leads to further changes in the lunar wake environment. Let us focus first on the specular model (panel *c*). We observe a dense plasma region at the bottom edge of the lunar wake followed by a rarefied plasma

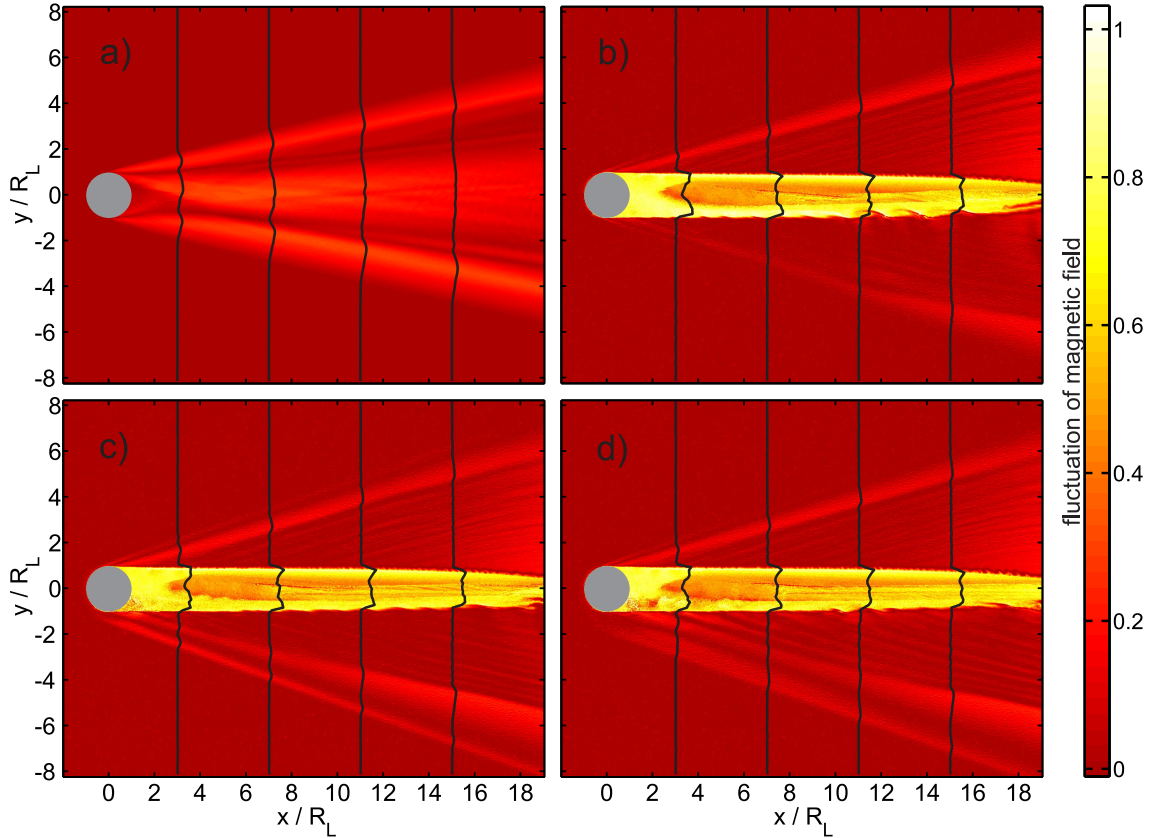


Figure 5.2: Magnetic field fluctuations $|\delta\mathbf{B}|$ for various simulation runs: Panel *a* represents the case with ambient magnetic field vectors lying in the simulation plane (i.e. initially $B_z = 0$). Other panels show the situation with ambient magnetic field vectors perpendicular to the simulation plane (i.e. initially $B_x = B_y = 0$) and different reflection models: without reflection (*b*), specular (*c*), and inverting (*d*). Right panel shows the corresponding scale. Overlaid curves denote several profiles of the density in arbitrary units.

region, which is larger than in previous cases. Another difference is the compression of bottom wave-dominated region in y -direction.

Using the inverting model (Figure 5.1d) leads to further changes in lunar wake. Namely, the region with relatively high density at the bottom edge of the wake is larger. Thus, the selected reflection model influences the global plasma environment. In other words, the global solar wind - Moon interaction is influenced by changes in the local microphysics of the reflection process.

Figure 5.2 shows the plots of **magnetic field fluctuations** $|\delta\mathbf{B}|$. In all cases we observe an enhancement of the magnetic field magnitude associated with the rarefied plasma regions. This behaviour is caused by the plasma effort to balance the pressure. The amplitude of magnetic field fluctuations in case *a* is higher than in the simulations with perpendicular ambient magnetic field. On the other hand, the situation in the center of lunar wake is

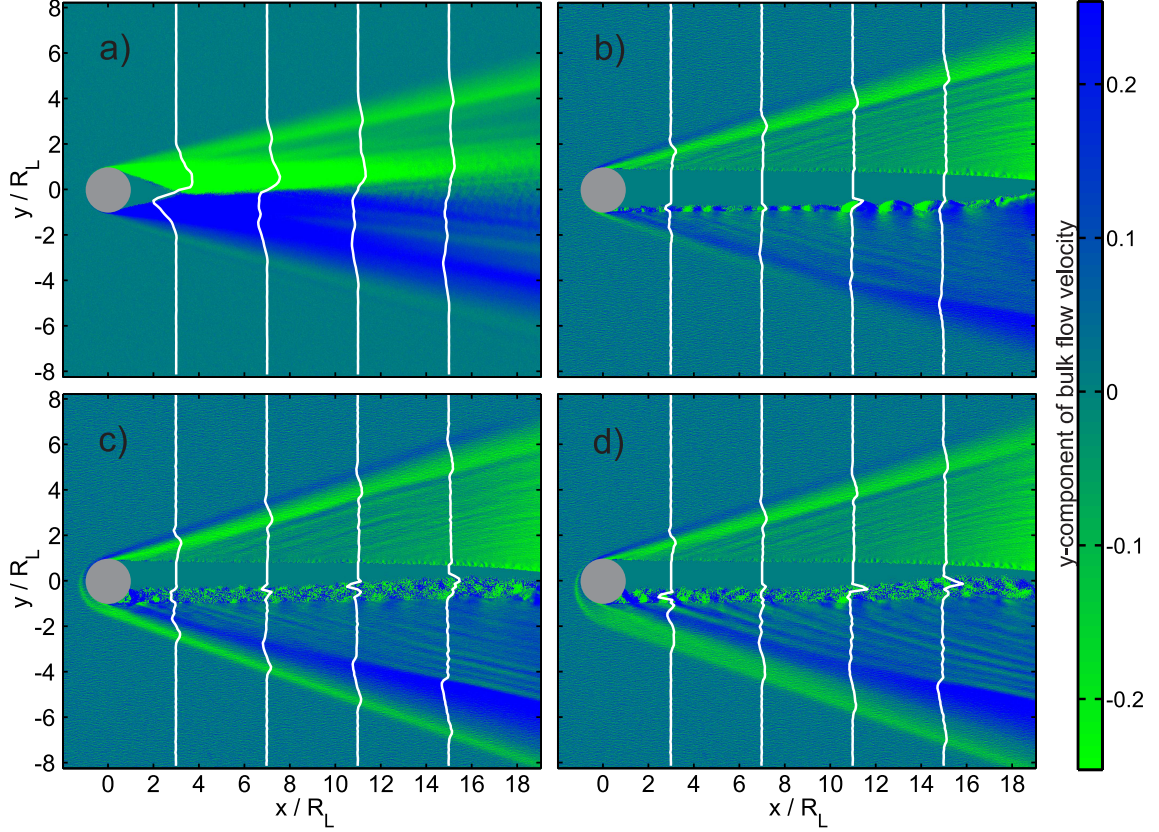


Figure 5.3: The y -component of plasma bulk flow velocity v_y for various simulation runs: Panel *a* represents the case with ambient magnetic field vectors lying in the simulation plane (i.e. initially $B_z = 0$). Other panels show the situation with ambient magnetic field vectors perpendicular to the simulation plane (i.e. initially $B_x = B_y = 0$) and different reflection models: without reflection (*b*), specular (*c*), and inverting (*d*). Right panel shows the corresponding scale. Overlaid curves denote several profiles of the density in arbitrary units.

reverse.

The increase of the magnetic field in the cavity in Figure 5.2 b - d can be explained in the following way [14]: The thermal pressure in the cavity is reduced, so that the magnetic field must increase in order to balance the ambient solar wind pressure. Let us put this rough argument on a quantitative footing. In the extreme case of a void cavity, the total pressure there is $\sim B_{cav}^2/2\mu_0$. Since $\beta_p = 1$, the thermal and magnetic pressure are equal in the ambient solar wind. Thus, the total pressure is $\sim B_{sw}^2/\mu_0$. Comparing these two values, we get

$$B_{cav} = \sqrt{2} B_{sw}. \quad (5.1)$$

Thus the magnetic field within the wake must increase by the factor of $\sqrt{2}$. This fact corresponds to the simulation results.

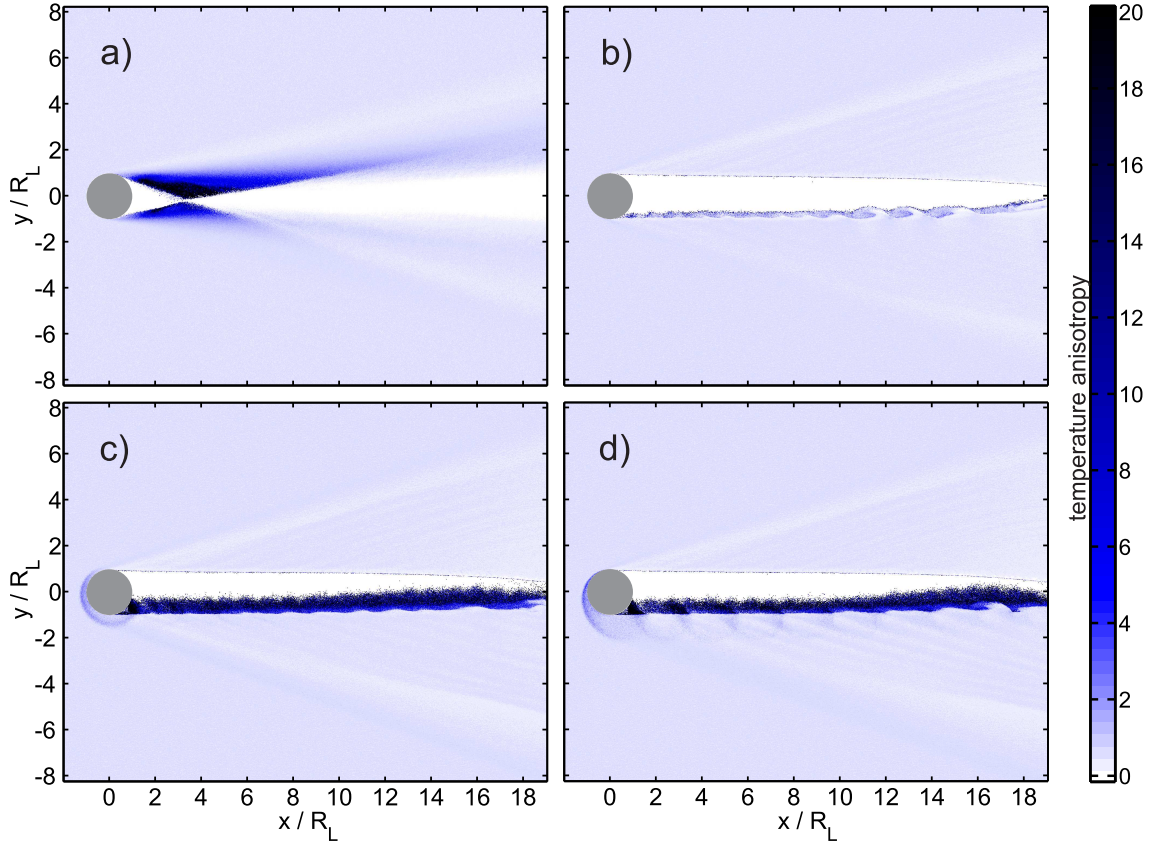


Figure 5.4: The proton temperature anisotropy $T_{\perp p}/T_{\parallel p}$ for various simulation runs: Panel *a* represents the case with ambient magnetic field vectors lying in the simulation plane (i.e. initially $B_z = 0$). Other panels show the situation with ambient magnetic field vectors perpendicular to the simulation plane (i.e. initially $B_x = B_y = 0$) and different reflection models: without reflection (*b*), specular (*c*), and inverting (*d*). Right panel shows the corresponding scale.

The **y-component of plasma bulk flow velocity** is shown in Figure 5.3. The blue color indicates the upward motion, whereas the green color denotes regions where plasma moves downward. In case *a*, the vertical projection of plasma bulk flow velocity in both upper and bottom half of the wake points to the center.

The situation in cases *b* - *d* is more complicated. We observe an interesting periodic effect at the bottom border of plasma cavity in *b*. This effect is related to the Larmor phase filtering by the Moon and is explained in Section 5.2. In simulations with proton reflections (bottom panels), the bottom edge of the lunar wake moves downward whereas the rest of the bottom half of the wake moves upward. It leads to large rarefied plasma region observed in Figure 5.1 c - d. The region of downward-moving plasma is larger in the inverting reflection model.

Figure 5.4 shows the **temperature anisotropy** for different configurations. In agree-

ment with [21], the cavity in case *a* is refilled with highly anisotropic plasma. It was shown in [21] that the anisotropy probably leads to low-frequency waves propagating in the direction antiparallel with respect to the magnetic field. We observe high temperature anisotropy at the borders of plasma cavity in case *b*. It may lead to instability resulting to generation of waves described in Section 5.2. In configurations with proton reflections, we see large regions of very high anisotropy. The areas correspond to the distribution of reflected protons. The enhancement of anisotropy was expected, as through the reflection process the proton thermal velocity in simulation plane increases from the value of $1v_A$ up to $10v_A$ (according to the reflection angle, see Section 5.4), whereas the thermal velocity in the z -direction remains unchanged.

5.2 Fourier analysis

In almost all global figures from the simulations with the perpendicular ambient magnetic field, we can see low-frequency waves propagating away from the lunar cavity. Let us focus on the magnetic fluctuations $\delta\mathbf{B}$ in Figure 5.2.

In order to process Fourier analysis of these waves, we have performed the simulation *d* (the most realistic one, as we will see in Section 5.5) with a longer total time, $t_{tot} = 110\omega_{qp}^{-1}$. The reason of such a long time is that we need to analyze larger waves-dominated rectangular area for longer time. We study the waves in the solar wind rest frame, in the bottom part of the lunar wake. Namely, we get the region $15R_L < x < 25R_L$, $-6R_L < y < -1R_L$ and the time interval $80\omega_{qp}^{-1} < t < 110\omega_{qp}^{-1}$. The time resolution is chosen to be $0.5\omega_{qp}^{-1}$.

The results of the analysis are presented in Figure 5.5. Left panel shows the fluctuations $\delta\mathbf{B}$ as a function of k_x and k_y averaged over all frequencies ω . The dependence of the fluctuations on k_x and the frequency ω is plotted in the right panel. The plot is averaged over all k_y . It follows that the frequency and the wavenumber of observed low-frequency waves are $\omega \approx 0.19\omega_{gp}^{-1}$ and $k \approx 0.14$, respectively. The resulting phase velocity $\omega/k \approx 1.35v_A$ and the fact that the waves propagate perpendicular to the magnetic field enable us to assume that the waves are magnetosonic waves with dispersion relation

$$\omega^2 = (v_s^2 + v_a^2)k^2, \quad (5.2)$$

where v_s is the speed of ion acoustic wave which in simulation units is

$$v_s = \sqrt{\frac{k_B T_e}{m_p}} = 1. \quad (5.3)$$

Thus, the phase speed of magnetosonic waves is $\omega/k = \sqrt{2}v_A$. It corresponds to the results of the Fourier analysis.

The generating mechanism is related to Larmor radius and thus it is a kinetic effect. We will describe it from the view of the rest frame. For illustration, let us focus on the protons having the guiding center at the level $y = -R_L$. According to the phase of the Larmor

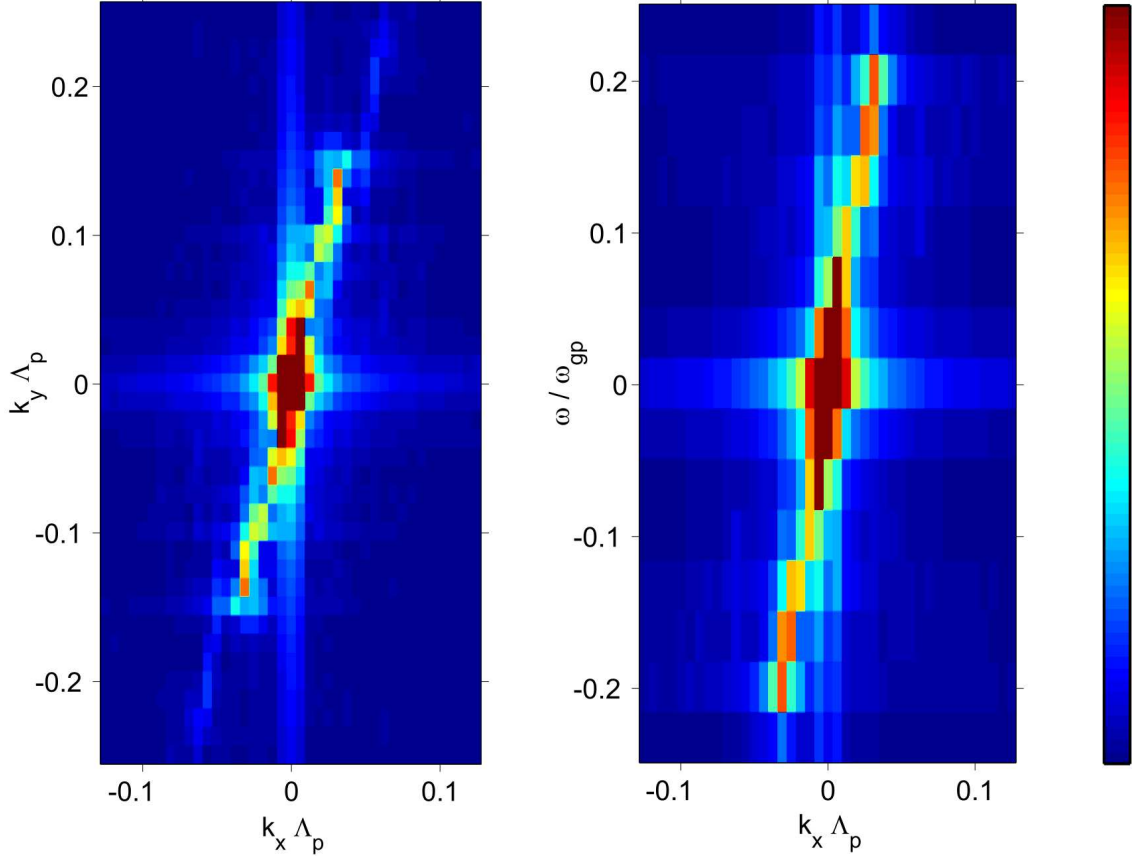


Figure 5.5: Fourier analysis of the magnetic fluctuations $\delta\mathbf{B}$ in region $15R_L < x < 25R_L$, $-6R_L < y < -1R_L$ and time interval $80\omega_{qp}^{-1} < t < 110\omega_{qp}^{-1}$. The left panel shows the fluctuations as a function of k_x and k_y (averaged over all frequencies ω). The right panel shows the fluctuations as a function of k_x and ω (averaged over all k_y). The frequency is given in the plasma rest frame.

motion, the proton is at the given moment located above or below this level. This location is important at the position $x = 0$ of the proton trajectory. Whereas the protons located here above the guiding center hit the lunar surface and are removed from the simulation, another protons continue in the motion. Note that the process is, in fact, more complex, because the Moon is placed not only at the position $x = 0$.

This Larmor phase filtering effect of the obstructing Moon leads to formation of a periodic structure along the cavity boundaries with the period $2\pi v_{sw}$. This periodicity leads to propagation of magnetosonic waves. The process is sketched in Figure 5.6. The wavenumber can be expressed by

$$k = \frac{\sqrt{2}}{4\pi v_A}. \quad (5.4)$$

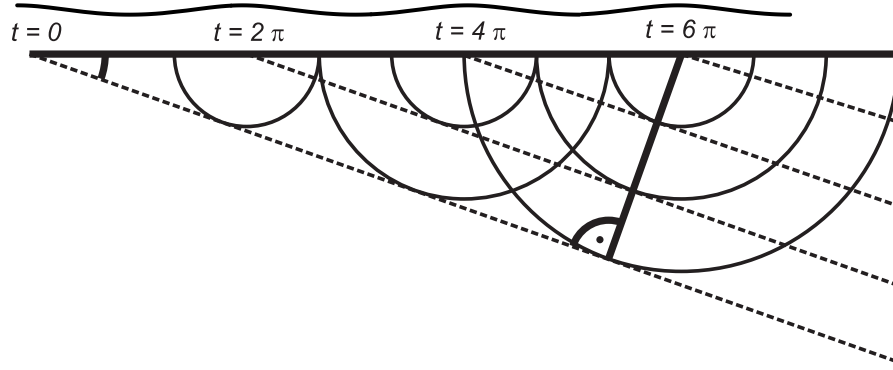


Figure 5.6: Sketch of the waves generating mechanism. A typical proton trajectory is plotted in the top.

The components of wavevector \mathbf{k} are then

$$k_x = \frac{1}{2\pi v_{sw}} \quad , \quad k_y = \frac{\sqrt{2}}{4\pi v_A} \sqrt{1 - \frac{2v_A^2}{v_{sw}^2}} \quad (5.5)$$

and the angle between equiphase lines of propagating waves and the x -axis

$$\cos \vartheta = \frac{\sqrt{2}v_A}{v_{sw}}. \quad (5.6)$$

If we put the parameters of our simulation to these relations, we get $k = 0.12$, $\mathbf{k} = (0.032, 0.11)$, and $\vartheta = 16.4^\circ$. These values correspond almost exactly to the simulation data (see Figure 5.5). Note that from the rest frame, view the waves look stationary and they do not propagate.

5.3 Reduced distribution functions

We study the distribution function around the cavity boundary and around some specific points denoted in Figure 5.7. All results are plotted in this figure. The bottom panel shows the reduced distribution function $f(x, v_y)$ along the southern edge of the cavity. In order to highlight maxima of the distribution function at each point $x = x_0$, we connect these points by a white curve.

For illustration, the velocity distributions in small neighborhoods around three specific points are plotted. Left panel shows the undisturbed Maxwellian distribution around a point outside the lunar wake structure. The central and right panels represent a typical bi-Maxwellian distribution at points located at the border of the cavity. The elliptic shape of the functions signalizes the existence of free energy at these locations which must be dissipated.

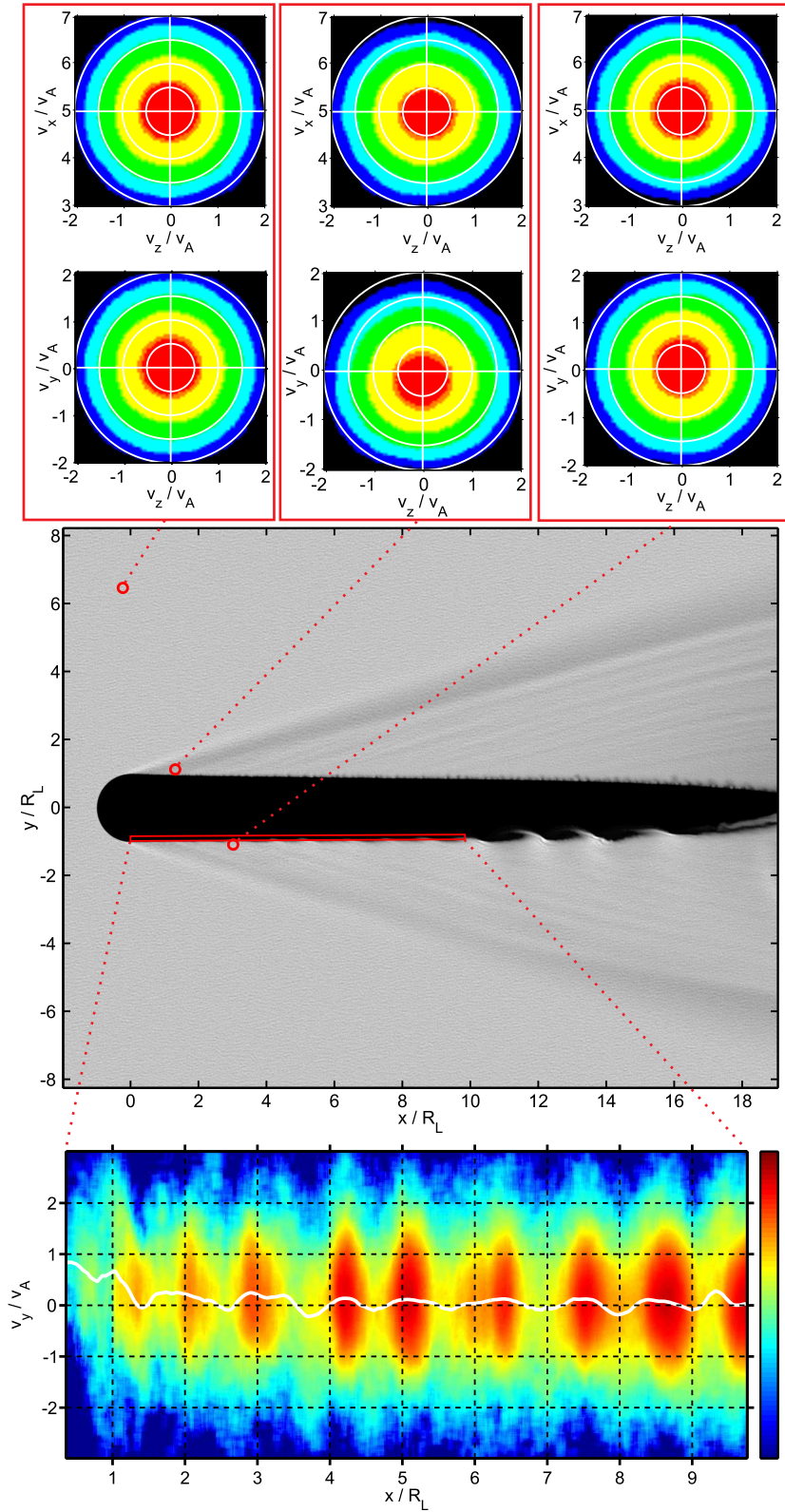


Figure 5.7: Reduced distribution functions $f(v_x, v_z)$ and $f(v_y, v_z)$ in various points of the simulation domain (top). Reduced distribution function $f(x, v_y)$ along the denoted line (bottom). White curve connects maximum points at every position $x = x_0$.

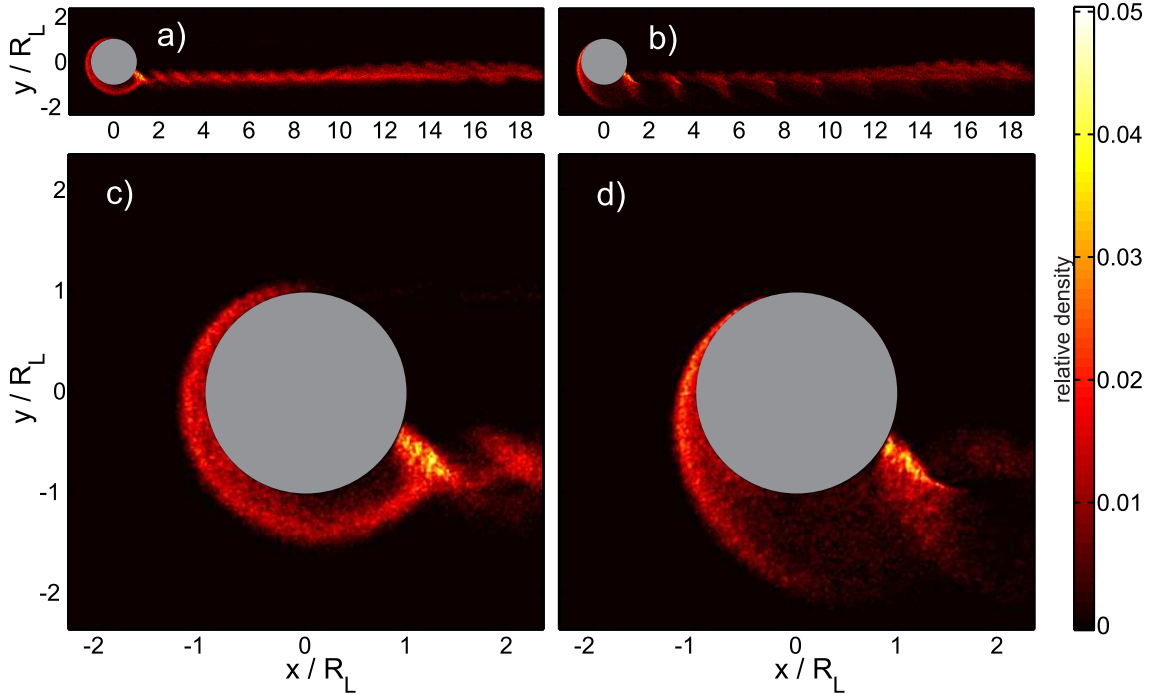


Figure 5.8: Different reflection processes. We show the reflected protons density for specular (a, c) and inverting (b, d) model. The values are scaled to the solar wind proton density.

5.4 Reflected protons

As explained in section 4.2, we have implemented proton reflections on the lunar surface. One percent of the protons impacting the lunar dayside are reflected without loss of kinetic energy (in the rest frame). Two different models prescribing how the reflection angle depends on the incidence angle were used. Let us now focus on the reflections in more detail.

Figure 5.8 shows the distribution of the density of reflected protons in both reflection models. There are significant differences in these plots according to used model. We see that the protons enter the near Moon wake and give rise to a strong asymmetry in this region. Whereas the southern hemisphere of the near-Moon wake is dominated by the reflected protons, they cannot reach the northern part. Note the cloud with a relatively high density of reflected protons approximately at the position $[R_L, -R_L]$. The formation of this region is explained below.

The dynamics of the reflected protons can be described in the following way. (The situation is sketched in Figure 5.9.) For simplicity, we assume the reflection at the equator, in the direction normal to the surface. First we look at the situation from the rest frame. The proton moves in the solar wind with the velocity of \mathbf{v}_{sw} . Then it is reflected on the lunar dayside surface (without loss of energy) and its velocity changes to $-\mathbf{v}_{sw}$. In the plasma frame, the velocity of its motion is equal to $-2\mathbf{v}_{sw}$ and the proton starts to gyrate counterclockwise with $r_g = (v_{sw}/v_A)\Lambda_p$. At the bottom part of its gyration, it has the

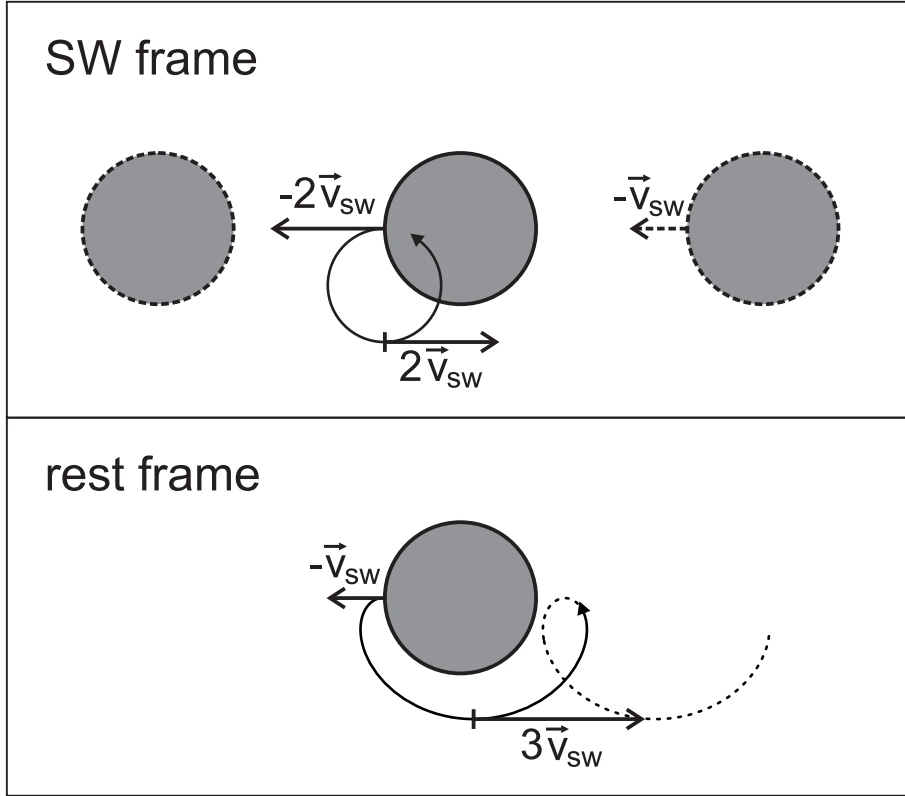


Figure 5.9: A growth of the kinetic energy of reflected protons. In the SW frame (top), the moon is moving with a velocity of $-v_{sw}$. The reflected proton starts to gyrate with initial speed $2v_{sw}$. From the rest frame view (bottom), the proton has a maximal speed ($3v_{sw}$) in bottom part of its trajectory. Hence the kinetic energy of reflected proton is up to 9 times greater than the one of ambient SW protons.

velocity of $2\mathbf{v}_{sw}$. If we now return to the rest frame, the velocity in that area reaches $3\mathbf{v}_{sw}$. Thus, the reflected protons obtain 9 times the original kinetic energy at this position. The magnitude of the velocity in the simulation plane varies according to the position at the cycloid trajectory as

$$v_{\perp} = v_{sw} [1 + 4\alpha(\alpha - \cos(\alpha t + \theta/2))]^{1/2} \quad , \quad \alpha = \cos \frac{\theta}{2} \quad (5.7)$$

where θ is the reflection angle according to the $(-x)$ -direction. It can be shown that for a given angle θ , the magnitude of the velocity of a reflected proton in simulation plane varies between values

$$v_{\perp min}(\theta) = v_{sw} |2 \cos(\theta/2) - 1| \quad , \quad v_{\perp max}(\theta) = v_{sw} |2 \cos(\theta/2) + 1| \quad (5.8)$$

When the proton reach the first loop of the trajectory, the magnitude of its velocity is minimal. This leads to the creation of regions with relatively high density of reflected protons observed in Figure 5.8.

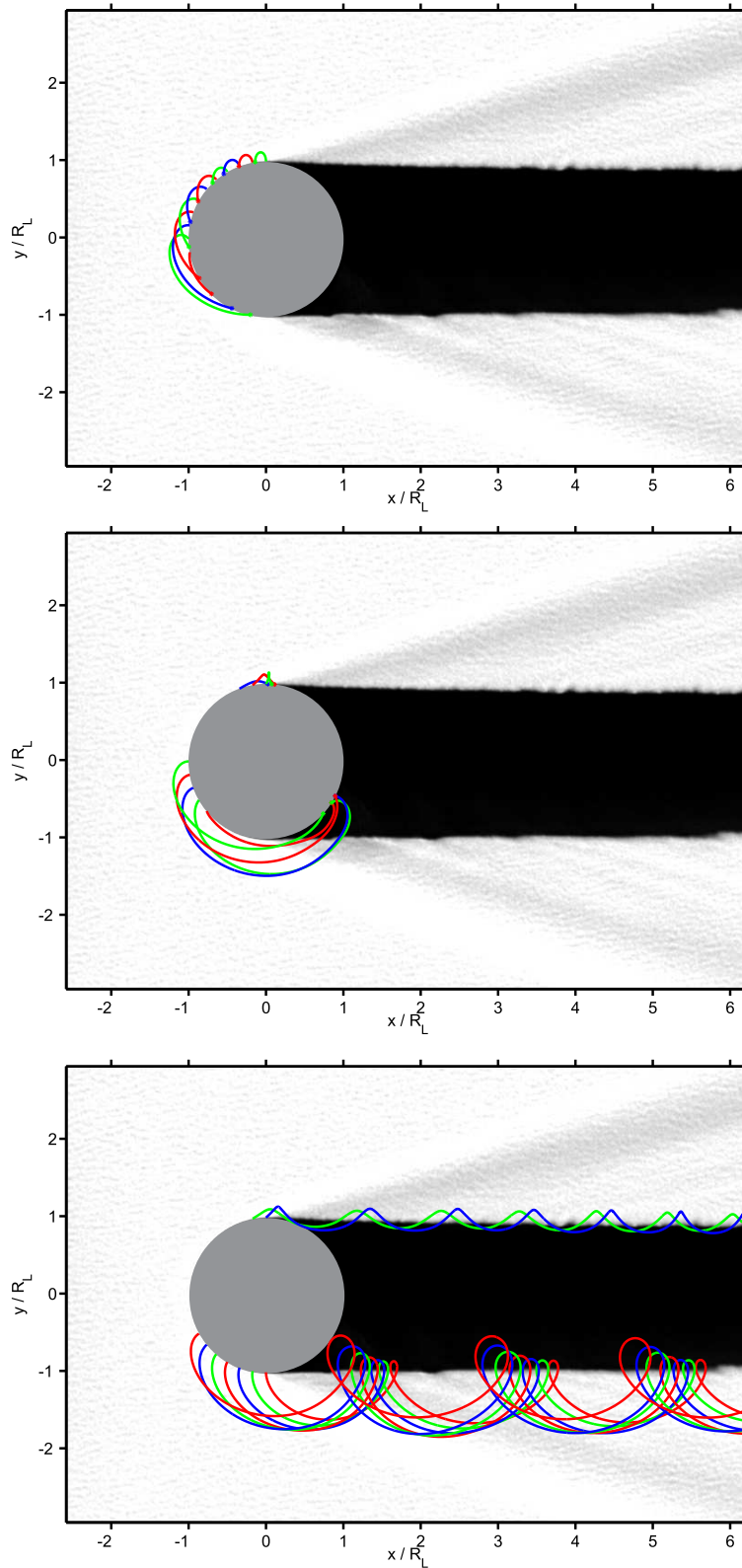


Figure 5.10: Examples of reflected protons trajectories according to their destination. Some of them hit the lunar surface again: on the dayside (top) or on the nightside (center). Others do not hit the surface again and continue in gyro-motion in solar wind flow direction (bottom).

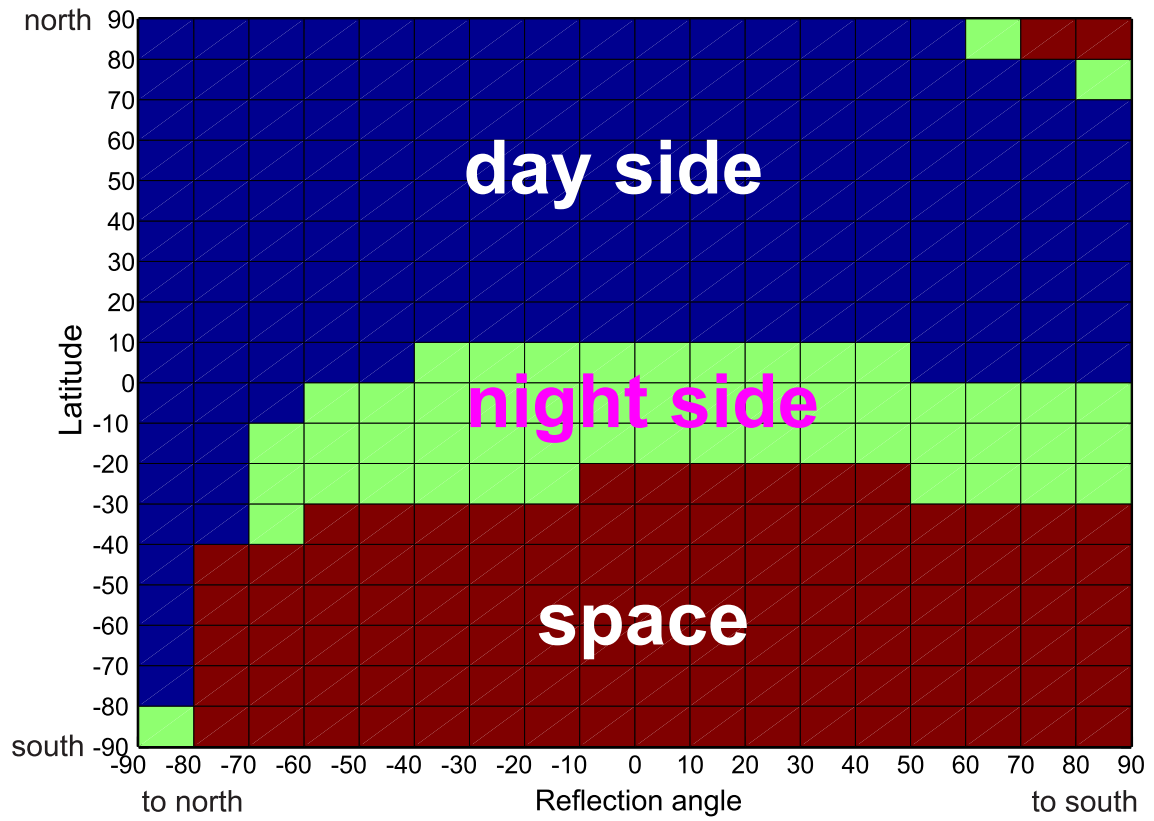


Figure 5.11: Destination of the reflected protons according to the position on the surface (vertical axis) and the reflection angle (horizontal axis).

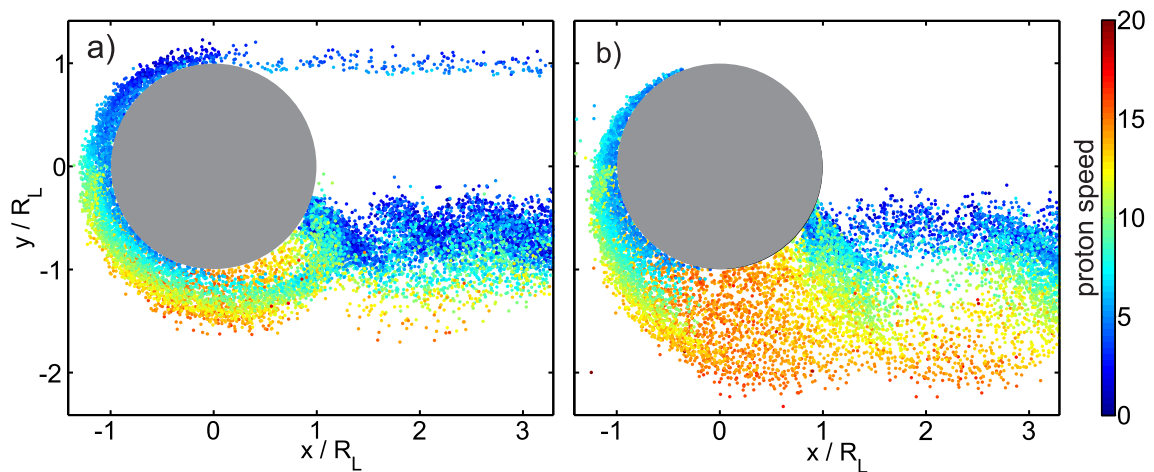


Figure 5.12: Some reflected proton superparticles, coloured by velocity magnitude.

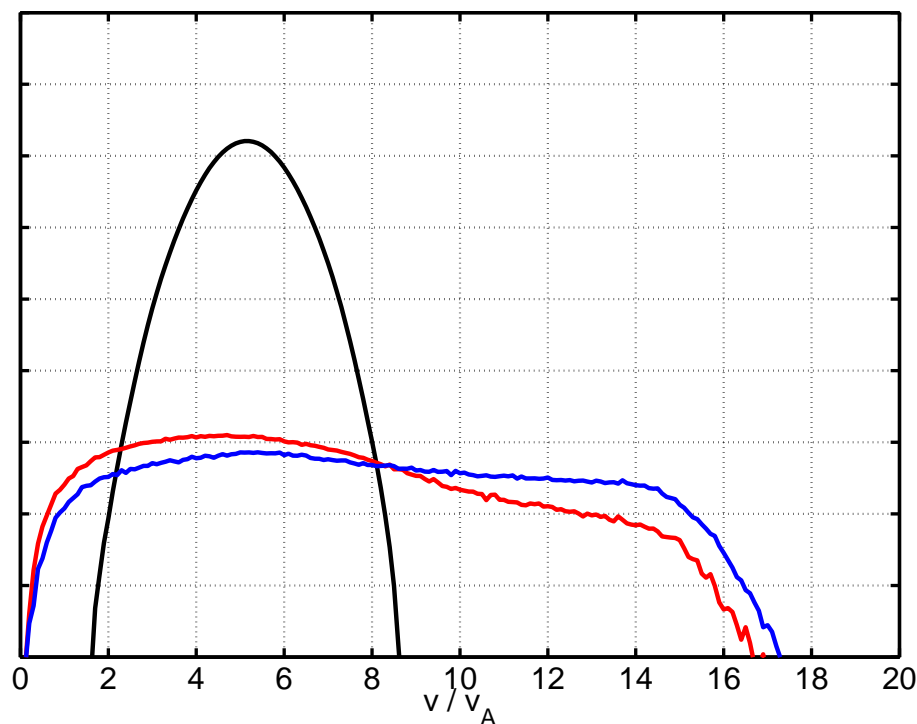


Figure 5.13: The velocity spectrum of all reflected protons in simulation domain: red - specular model, blue - inverting model. Black line corresponds to the solar wind protons. The y-axis scale is logarithmic in arbitrary units.

The examples of trajectories are plotted in Figure 5.10. There are three possible destinations of reflected protons depending on the position and the angle of the reflection: they can hit the dayside again, or they can impact the nightside, or, finally, they can continue in gyro-motion with the solar wind bulk speed.

Figure 5.11 shows the destination of the reflected protons according to the latitude and reflection angle. The protons which hit the nightside surface have been reflected on south hemisphere near equator. Contrary to this, the protons reflected on the north hemisphere often hit the dayside surface again. The protons reflected on other places most probably do not hit the lunar surface again.

Figure 5.12 shows some reflected protons superparticles, colored by velocity magnitude. The acceleration along the motional electric field is clearly visible.

To illustrate the sensitivity of the reflected protons to the microphysics of the reflection process, we show in Figure 5.13 how the velocity space distributions of the reflected protons change if we use the specular or the inverting reflection model. The red line corresponds to the specular model, whereas the inverting model is represented by the blue line. The solar wind protons are plotted by the black line. The velocity distributions of the reflected protons

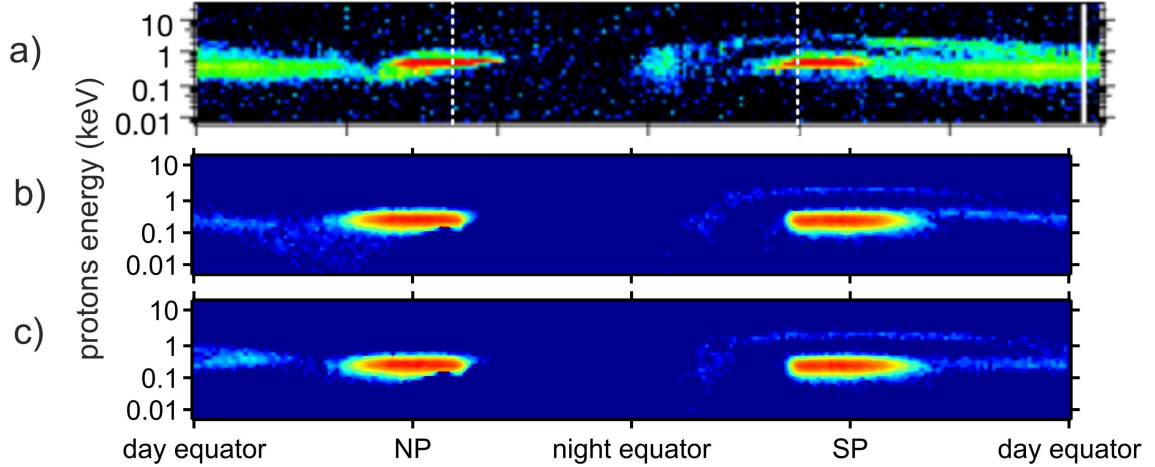


Figure 5.14: Comparison of experimental data from SELENE (Kaguya) with simulation data. Energetic ion spectrum taken during one orbit by Kaguya (a) (adopted from [16]). Simulation data taken along a virtual spacecraft orbit for specular (b) and inverting (c) reflection model.

are much broader. This fact corresponds to in-situ measurements from Chandrayaan 1 (see [9, Figure 1]).

The difference between the red and the blue line can be explained in the following way. It follows from (5.8) that the average velocity of the reflected protons decrease with the increasing angle θ . In the case of the inverting model, the angle θ of the reflected protons nears to zero regardless the impact position. Thus, the speed of all reflected protons varies approximately from v_{sw} to $3v_{sw}$. When we look at the specular model, the angle θ increases with increasing distance of the impact point from the equator. Therefore, there are more reflected protons with higher speed when using inverting reflection model.

5.5 Comparison with data from Kaguya

The Japanese spacecraft SELENE (Kaguya) orbited the Moon at ~ 100 km altitude in polar orbit. One of the instruments onboard (IMA) faced the lunar surface to measure upgoing ions with a half-sphere field of view. Although IMA was constructed to measure ions reflected on the lunar surface, it also detected SW ions around the day-night terminator because of its large field of view. The range of measured energies per charge is between 7 eV/q and 29 keV/q. As the time resolution of IMA was 32 sec, it made over 220 measurements during one 2-hour period.

In order to verify the relevance of our simulation model, we let a virtual spacecraft fly through our simulation plane at ~ 100 km $\approx 1\Lambda_p$ altitude and measure up-going protons. Then we compare the resulting data with real in-situ observations. In fact, we take a ring

of inner radius Λ_p and outer radius $1.4\Lambda_p$ and divide it into 220 slices. We sum all protons in each slice and sort it according to their kinetic energy.

The results are plotted in Figure 5.14. Top panel shows the real in-situ measurement of Kaguya. The flight of our virtual spacecraft begins above the equator on the dayside and continues to the north. Here it detects only protons reflected from the surface. Around the north pole, the solar wind protons are detected. Therefore there is a growth of the measured particles number. No particles reach the north part of the nightside. Then, below the equator, the spacecraft starts to detect protons reflected on the dayside and accelerated by the motional electric field. The detection of solar wind protons around the south pole follows again. In the south part of sunward side we can see both the protons reflected from the surface and those reflected further north from the detection place and accelerated by the electric field.

Middle panel corresponds to the specular reflection model. We observe a detection of low-energy protons in the left part of the spectrum plot. Such protons are not present in real measurement. It indicates that the inverting reflection model (bottom panel) is more realistic than the specular one.

Chapter 6

Conclusions

We have studied the phenomena associated with the solar wind proton reflections on the lunar surface using different initial and boundary parameters. We have performed several numerical simulations using a two-dimensional hybrid code. The results provide a global view to the in-situ observations.

We have demonstrated the influence of the magnetic field direction upon the shape of the lunar wake. Some interesting physical effects are exhibited in simulation results. We observe the creation of waves propagating away from the center of the lunar wake. The Fourier analysis showed that the wavenumber $k = 0.13$ and the frequency $\omega = 0.18\omega_{qp}$. Since the waves propagate perpendicular to the magnetic field lines with the velocity $\approx \sqrt{2}v_A$, we expect that they are magnetosonic waves.

We have described the generating mechanism of the waves. It is related to the Larmor phase filtering effect by the obstructing Moon. It results in the periodic structure of plasma along the borders of plasma-depleted cavity downstream the Moon. Such a configuration is unstable and leads to energy dissipation through magnetosonic waves. We have derived the expected wavenumber $k = \sqrt{2}/(4\pi v_A) = 0.12$ and the angle between equiphase lines of propagating waves and the x -axis $\vartheta = \arccos(\sqrt{2}v_A/v_{sw}) = 16.4^\circ$.

We have plotted the reduced distribution function $f(x, v_y)$ along the cavity boundary to demonstrate the periodic structure of plasma in this region in more detail. The anisotropic velocity distribution was plotted in some points at this boundary.

In other two simulations we have implemented to the code proton reflections on the lunar surface. One percent of the impacted protons is reflected without loss of energy. We used two reflection models: the specular model and the inverting model. The former assumes that the Moon behaves like an ideal sphere, whereas in the latter all protons are reflected contrary to the incidence direction.

We have showed that the introduction of the proton reflections changes the shape of the lunar wake. The reflected protons are picked-up by the solar wind, accelerated by the motional electric field to obtain up to 9 times the original kinetic energy, and then they penetrate into the near-Moon wake, leading to asymmetry of the lunar plasma environment. We observe a region with relatively high density of reflected protons below the nightside

sub-solar point associated with a trajectory loop. We have demonstrated that the protons reflected to the south of the equator may hit the lunar nightside surface.

We have compared the simulation data with in-situ observations of Japanese spacecraft SELENE (Kaguya). The comparison of two reflection models with real data follows that the inverting model is more realistic than the specular one.

There are several directions how to extend the research of lunar wake. First of all, the full three-dimensional model will give more realistic results. We can also include alpha particles into the simulation, which were neglected in present thesis. It will be interesting to verify the simulation results with real data from ARTEMIS mission, in which two spacecrafts orbit at various altitudes. In order to fit the simulation to the real data, the more appropriate reflection model will be required.

Appendix A

Constants and values

Constants used in the text:

$\epsilon_0 = 8.854187817 \cdot 10^{-12} \text{ F m}^{-1}$ - free space permittivity

$\mu_0 = 1.256637061 \cdot 10^{-6} \text{ N A}^{-2}$ - free space susceptibility

$k_B = 1.3806504 \cdot 10^{-23} \text{ J K}^{-1}$ - Boltzmann constant

$m_e = 9.10938215 \cdot 10^{-31} \text{ kg}$ - electron mass

$m_p = 1.672621637 \cdot 10^{-27} \text{ kg}$ - proton mass

$e = 1.602176487 \cdot 10^{-19} \text{ C}$ - electron (proton) charge

$c = 2.99792458 \cdot 10^8 \text{ m s}^{-1}$ - free space speed of light

Bibliography

- [1] Baumjohann, W., and Treumann, R., "Basic Space Plasma Physics", Imperial College Press, 1997.
- [2] Birch, P. C., and S. C. Chapman (2001), Detailed Structure and Dynamics in Particle-in-Cell Simulations of the Lunar Wake. *Physics of Plasmas* 8, 10.
- [3] Bosqued, J. M., et al. (1996), Moon-solar wind interactions: First results from the WIND/3DP Experiment, *Geophys. Res. Lett.*, 23(10), 1259–1262.
- [4] Farrell, W. M., R. J. Fitzenreiter, C. J. Owen, J. B. Byrnes, R. P. Lepping, K. W. Ogilvie, and F. Neubauer (1996), Upstream ULF waves and energetic electrons associated with the lunar wake: Detection of precursor activity, *Geophys. Res. Lett.*, 23(10), 1271–1274.
- [5] Farrell, W., M. Kaiser, J. Steinberg, and S. Bale (1998), A simple simulation of a plasma void: Applications to Wind observations of the lunar wake, *J. Geophys. Res.*, 103(A10), 23653–23660.
- [6] Freeman, J. W., Jr. (1972), Energetic ion bursts on the nightside of the moon, *J. Geophys. Res.*, 77, 239–243, doi: 10.1029/JA077i001p00239.
- [7] Futaana, Y., S. Barabash, M. Wieser, M. Holmström, A. Bhardwaj, M. B. Dhanya, R. Sridharan, P. Wurz, A. Schaufelberger, K. Asamura (2010), Protons in the near-lunar wake observed by the Sub-keV Atom Reflection Analyzer on board Chandrayaan-1, *J. Geophys. Res.*, 115, A10248, doi:10.1029/2010JA015264
- [8] Hellinger, P., P. Trávníček, J. C. Kasper, and A. J. Lazarus (2006), Solar wind proton temperature anisotropy: Linear theory and WIND/SWE observations, *Geophys. Res. Lett.*, 33, L09101, doi:10.1029/2006GL025925.
- [9] Holmström, M., M. Wieser, S. Barabash, Y. Futaana, and A. Bhardwaj (2010), Dynamics of solar wind protons reflected by the Moon, *J. Geophys. Res.*, 115, A06206, doi:10.1029/2009JA014843
- [10] Kallio, E. (2005), Formation of the lunar wake in quasi-neutral hybrid model, *Geophys. Res. Lett.*, 32, L06107, doi:10.1029/2004GL021989.

- [11] Kellogg, P. J., K. Goetz, and S. J. Monson (1996), Observations of plasma waves during a traversal of the Moon’s wake, *Geophys. Res. Lett.*, 23(10), 1267–1270, doi:10.1029/96GL00376.
- [12] Matthews, A. P. (1994), Current Advance Method and Cyclic Leapfrog for 2D Multi-species Hybrid Plasma Simulations, *J. Comp. Phys.*, 112, 102–116.
- [13] Meyer-Vernet, N., ”Basics of the solar wind“, Cambridge University Press, 2007.
- [14] Ness, N. F., K. W. Behannon, C. S. Scarce, and S. C. Cantarano (1967), Early Results from the Magnetic Field Experiment on Lunar Explorer 35, *J. Geophys. Res.*, 72(23), 5769–5778, doi:10.1029/JZ072i023p05769.
- [15] Nishino, M. N., K. Maezawa, M. Fujimoto, Y. Saito, S. Yokota, K. Asamura, T. Tanaka, H. Tsunakawa, M. Matsushima, F. Takahashi, T. Terasawa, H. Shibuya, and H. Shimizu (2009), Pairwise energy gain-loss feature of solar wind protons in the near-Moon wake, *Geophys. Res. Lett.*, 36, L12108, doi:10.1029/2009GL039049.
- [16] Nishino, M. N., M. Fujimoto, K. Maezawa, Y. Saito, S. Yokota, K. Asamura, T. Tanaka, H. Tsunakawa, M. Matsushima, F. Takahashi, T. Terasawa, H. Shibuya, and H. Shimizu (2009), Solar-wind proton access deep into the near-Moon wake, *Geophys. Res. Lett.*, 36, L16103, doi:10.1029/2009GL039444.
- [17] Oglivie, K. W., J. T. Steinberg, R. J. Fitzenreiter, C. J. Owen, A. J. Lazarus, W. M. Farrell, and R. B. Torbert (1996), Observations of the lunar plasma wake from the WIND spacecraft on December 27, 1994, *Geophys. Res. Lett.*, 23, 1255–1258.
- [18] Saito, Y., et al. (2008), Solar wind proton reflection at the lunar surface: Low energy ion measurement by MAP-PACE onboard SELENE (KAGUYA), *Geophys. Res. Lett.*, 35, L24205, doi:10.1029/2008GL036077.
- [19] Shubert, G., and B. R. Lichtenstein (1974), Observations of moon-plasma interactions by orbital and surface experiments, *Rev. Geophys. and Space Phys.*, 12, 592–626.
- [20] Trávníček, P., P. Hellinger, and D. Schriver (2007), Structure of Mercury’s magnetosphere for different pressure of the solar wind: Three dimensional hybrid simulations, *Geophys. Res. Lett.*, 34, L05104, doi:10.1029/2006GL028518.
- [21] Trávníček, P., and P. Hellinger (2005), Structure of the lunar wake: Two-dimensional global hybrid simulations, *Geophys. Res. Lett.*, 32, L06102, doi:10.1029/2004GL022243.
- [22] Wieser, M., S. Barabash, Y. Futaana, M. Holmstrom, A. Bhardwaj, R. Sridharan, M. B. Dhanya, P. Wurz, A. Schaufelberger, K. Asamura (2009), Extremely high reflection of solar wind protons as neutral hydrogen atoms from regolith in space, *Planetary and Space Science*, 57(14–15), 2132–2134.